POLITECNICO DI TORINO
Repository ISTITUZIONALE

Influence of Pr-doping on the sulfur tolerance of Pd-ceria catalysts for complete methane oxidation

Original
Influence of Pr-doping on the sulfur tolerance of Pd-ceria catalysts for complete methane oxidation / Sartoretti, E., Calì, E., Novara, C., Giorgis, F., Piumetti, M., Fino, D., Russo, N., Bensaid, S.. - In: APPLIED CATALYSIS. B, ENVIRONMENTAL. - ISSN 0926-3373. - ELETTRONICO. - 404:(2027), pp. 1-17. [10.1016/j.apcatb.2026.127701]

Availability:
This version is available at: 11583/3017292 since: 2026-10-31T13:56:19Z

Publisher:
Elsevier

Published
DOI:10.1016/j.apcatb.2026.127701

Terms of use:

This article is made available under terms and conditions as specified in the corresponding bibliographic description in the repository

Publisher copyright

(Article begins on next page)

19 November 2026

Applied Catalysis B: Environment and Energy 404 (2027) 127701



Contents lists available at ScienceDirect

Applied Catalysis B: Environment and Energy

journal homepage: www.elsevier.com/locate/apcatb



Influence of Pr-doping on the sulfur tolerance of Pd-ceria catalysts for complete methane oxidation

Enrico Sartoretti *, Eleonora Calì, Chiara Novara, Fabrizio Giorgis, Marco Piumetti, Debora Fino, Nunzio Russo, Samir Bensaid

Department of Applied Science and Technology, Politecnico di Torino, Corso Duca degli Abruzzi, 24, Turin, 10129, Italy

A R T I C L E I N F O

Keywords:
Catalytic methane oxidation
Palladium/ceria catalysts
Praseodymium-doped ceria
Sulfur poisoning
Metal-support interaction
Deactivation
Regeneration

A B S T R A C T

In this work, the influence of praseodymium doping on the sulfur tolerance of Pd/CeO_2 catalysts for total methane oxidation was systematically investigated. Pd catalysts supported on nanostructured ceria, praseodymia, and mixed oxides (10 or 50 at% Pr) were exposed to SO_2 (20 ppm) under dry or wet reaction conditions, followed by high-temperature regeneration cycles up to 900 °C. The Pr loading strongly affected the sulfur-catalyst interactions. Undoped Pd/CeO_2 underwent fast deactivation due to preferential sulfation of Pd particles, although sulfates were almost completely removed during thermal treatment. In contrast, Pr-doped catalysts exhibited enhanced sulfur resistance, as sulfur preferentially accumulated on the support rather than on Pd. Mild Pr doping (10 at%) provided the best compromise, ensuring limited sulfate accumulation and effective regeneration under the investigated conditions, while preserving the ability of Pr to stabilize PdO species at high temperature, even in the presence of water. Higher Pr loadings promoted extensive sulfate formation, which resulted in Pr segregation from the ceria lattice, weakening of Pd-support interactions, and Pd sintering on pure praseodymia; moreover, sulfates were not completely removed upon regeneration but reorganized into stable bulk aggregates, inducing structural distortion. These results demonstrate that controlled Pr doping effectively tunes sulfur affinity and metal-support interactions, providing useful guidelines for the design of sulfur-tolerant Pd-based catalysts for methane oxidation.

1. Introduction

Today, natural gas is increasingly employed in power generation plants and in the transportation field, due to its lower emissions of CO_2, NO_x, SO_x and particulate matter compared with conventional liquid fuels [1]. For instance, the use of liquefied natural gas (LNG) and bio-LNG has recently emerged as an attractive option in the maritime sector, to comply with increasingly stringent emission legislations, such as the FuelEU Maritime initiative or the IMO 2020 Global Sulfur Cap and Tier III NO_x limits set by the International Maritime Organization [2,3]. Methane is also considered a strategic energy carrier and feedstock for hydrogen production and, besides being the main component of natural gas, can be produced through renewable pathways, including biomethane from biogas upgrading and synthetic methane produced from renewable H_2 and captured CO_2 [4–6]. However, the environmental benefits of natural gas may be partially offset by methane slip, i.e., the emission of unburned CH_4 in exhaust gases, which remains a major concern because methane exhibits a significantly higher global warming potential than carbon dioxide [7]. Catalytic oxidation to CO_2 is currently one of the most effective strategies for methane abatement, making the development of efficient and durable catalytic systems essential for both stationary and mobile applications [8].

Among the possible catalysts for complete methane oxidation, supported Pd-based materials are widely recognized as the most effective at low temperatures [9,10]. Nevertheless, the nature of the active sites in these catalysts remains a subject of debate [11]. PdO has long been considered the primary active species, generally operating through a Mars-van Krevelen-like mechanism, but recent studies increasingly point to a dynamic active state involving the coexistence of Pd^0 and PdO_x species alongside the formation of highly reactive metal/oxide interfacial sites [12–16]. In this context, ceria-based supports are particularly attractive because their redox properties and oxygen storage-release capability can promote the reoxidation of palladium and stabilize catalytically relevant PdO_x structures through strong

* Corresponding author.
E-mail address: enrico.sartoretti@polito.it (E. Sartoretti).

https://doi.org/10.1016/j.apcatb.2026.127701
Received 24 July 2026; Received in revised form 8 October 2026; Accepted 27 October 2026
Available online 27 October 2026
0926-3373/© 2026 The Author(s). Published by Elsevier B.V. This is an open access article under the CC BY-NC-ND license (http://creativecommons.org/licenses/by-nc-nd/4.0/).

metal-support interactions [17–19]. At the same time, the efficient use of palladium and the control of its interaction with ceria remain crucial for achieving both high activity and long-term durability [20,21].

Despite their high intrinsic activity, Pd-based catalysts are severely affected by deactivation under operation [22,23]. Water vapor, an unavoidable combustion product, typically causes a rapid but largely reversible inhibition by promoting hydroxyl accumulation and, at relatively low temperature, the formation of inactive hydroxylated palladium species [24,25]. A much more critical issue is sulfur poisoning, originating from trace sulfur compounds such as H_2S, COS or SO_2 that may be present in natural gas, biogas, and odorized fuels. Sulfur species can adsorb on palladium sites, hinder methane activation, and lead to the formation of thermodynamically stable sulfates, including inactive $PdSO_4$ [26]. In parallel, sulfur can spill over to the oxide support, where stable sulfur-containing surface and bulk species may form, making regeneration increasingly difficult after prolonged exposure [27].

Several strategies have been proposed to mitigate sulfur-induced deactivation [22,28]. One approach relies on using supports with significant sulfur-storage capacity, such as alumina, ceria or zirconia, which can act as preferential sulfur acceptors and temporarily protect Pd sites [17,29]. However, excessive sulfur uptake may also promote the formation of stable support sulfates and hinder full regeneration. A complementary method consists in tailoring the surface properties of the support to limit the adsorption and stabilization of sulfur species, e.g. by tuning its acidity/basicity or by modifying the near-surface composition [30]. For instance, Yang et al. reported that a moderate addition of silicates to ceria-zirconia enhanced methane oxidation activity by modulating electron transfer from the support to palladium, while maintaining a proper quantity of support sacrificial sites for SO_2 adsorption, which can hinder sulfur poisoning of palladium [31]. Ding et al. even reported an unexpected beneficial effect of sulfation on $Pd/Ce_{0.5}Zr_{0.5}O_2$, which was attributed to the higher acidity of the support and to the formation of sulfate species at the Pd-support interface, which can promote the dissociative adsorption of methane [32]. These observations demonstrate that support composition can profoundly affect sulfur chemistry and catalyst performance, suggesting that modifications that can alter support redox properties, acidity, and metal-support interactions may also strongly influence sulfur tolerance.

Among the different pathways explored to promote Pd/CeO_2-based methane oxidation catalysts, praseodymium doping has recently emerged as a promising route to improve catalytic performance, especially under wet conditions [33–35]. Pr addition can indeed modify the Pd oxidation state, the hydrophilic/hydrophobic balance of the support, and the strength of metal-support interactions, leading to improved activity when moderate Pr amounts are used. Instead, excessive Pr loadings stabilize overly oxidized Pd species and hinder catalytic activity. However, although the beneficial role of Pr under wet methane oxidation has been established, its effect on sulfur-induced deactivation has not yet been investigated. Key aspects that remain unknown include the influence of Pr content on sulfur uptake by Pd and the support, the formation and stability of sulfur-containing species, their effect on the catalytic activity over time, and the possibility of catalyst regeneration at high temperatures.

To address this knowledge gap, the present work elucidates the influence of praseodymium doping on the sulfur tolerance and thermal regeneration behavior of Pd/ceria catalysts for complete methane oxidation. Pd catalysts supported on nanostructured ceria, praseodymia, and mixed Ce-Pr oxides were exposed to SO_2 under reaction conditions and subsequently subjected to high-temperature regeneration. By combining catalytic testing with complementary characterization techniques, the effects of Pr loading on sulfur uptake, sulfate stability, and on the structural/chemical evolution of the catalysts were investigated. The results provide fundamental understanding of the mechanisms governing sulfur poisoning and regeneration in Pd/Ce-Pr systems, offering valuable insights for the rational design of sulfur-tolerant methane oxidation catalysts.

2. Materials and methods

2.1. Catalyst preparation

Nanostructured supports based on ceria, praseodymia, and two ceria-praseodymia solid solutions were prepared via a hydrothermal route, following a procedure adapted from a previous work [34]. In a typical synthesis, appropriate amounts of $Ce(NO_3)_3{\cdot}6\ H_2O$ (99.99%, Sigma-Aldrich) and/or $Pr(NO_3)_3{\cdot}6\ H_2O$ (99.9%, Sigma-Aldrich) were dissolved in 9 mL of deionized water to obtain a total amount of 20 mmol of metal cations, with the Ce/Pr molar ratio adjusted according to the desired support composition. Separately, 48 g of NaOH (98%, Sigma-Aldrich) were dissolved in 70 mL of deionized water. The nitrate solution was then added dropwise to the NaOH solution under continuous stirring. The resulting suspension was stirred at room temperature for 1 h and subsequently transferred to a Teflon-lined stainless-steel autoclave, where it was aged at 180 °C for 24 h. After the hydrothermal treatment, the precipitate was recovered by repeated centrifugation and washed several times with ethanol and deionized water until the washing solution reached neutral pH, in order to remove residual NaOH. The solid was then dried overnight at 60 °C, gently ground in a mortar, and calcined in static air at 650 °C for 4 h. The thus-obtained oxides were denoted as Ce(100 − X)Pr(X), where X indicates the nominal atomic percentage of Pr relative to total rare-earth content Ce + Pr (X = 0, 10, 50, 100).

Supported palladium catalysts were prepared by incipient wetness impregnation, targeting a nominal Pd loading of 2 wt%. For each sample, 1.5 g of ceria/praseodymia support was placed in a ceramic crucible and heated to 150 °C on a heating plate. An aqueous $Pd(NO_3)_2$ solution (99.99%, Sigma-Aldrich), containing the amount of precursor required to achieve the target Pd loading, was then gradually added dropwise to the support. The impregnated materials were finally calcined in static air at 900 °C for 4 h and labelled as Pd/Ce(100–X)Pr(X). A high calcination temperature was selected to thermally stabilize the catalysts at the maximum temperature subsequently reached during the catalytic tests, thereby limiting major structural rearrangements during the reaction cycles.

2.2. Catalyst characterization

The elemental composition of the Pd-containing samples was determined by inductively coupled plasma–mass spectrometry (ICP-MS), using a Thermo Scientific iCAP RQ. For the analysis, the solid powder was digested at 200 °C for 30 min in a mixture of HNO_3, HCl, and H_2O_2.

Textural properties were assessed via N_2 physisorption at −196 °C using a Micromeritics Tristar II 3020 apparatus. Prior to measurement, samples were outgassed under N_2 flow at 200 °C for 2 h. The specific surface area was calculated through the Brunauer-Emmett-Teller (BET) method.

The crystalline structure was investigated by powder X-ray diffraction (XRD) in a Malvern Panalytical Empyrean III, employing Cu Kα radiation (λ = 1.5419 Å). XRD patterns were collected over a 20 – 80° 2θ range, with a step size of 0.013° and a dwell time of 90 s per step. Peak assignment was carried out using the ICDD database, while average crystallite size was derived from the Debye-Scherrer equation, correcting for instrumental broadening with a LaB_6 standard.

Raman spectroscopy was performed by a Renishaw InVia micro-Raman system equipped with a cooled CCD detector and a 514.5 nm excitation laser (1 mW power). For each material, three spectra at room temperature were collected in different regions with a 5x objective and a 225 s total acquisition time.

To study the morphology of the catalysts, a Zeiss Merlin field-emission scanning electron microscope (FESEM), equipped with a

Gemini-II column, was employed. An Oxford X-act detector was used to evaluate the elemental composition of fresh and spent samples through energy dispersive X-ray spectroscopy (EDX), collecting spectra in at least 4 different areas and averaging the results.

High-resolution micrographs were also recorded in a Thermo Scientific Talos F200X transmission electron microscope (TEM), operated at 200 kV. The elemental distribution in fresh and spent samples was investigated by collecting EDX maps, in scanning transmission electron microscopy (STEM) mode. Selected HR-TEM images were acquired at the HoloTEM facility of the University of Salento using a JEOL JEM-ARM200F NEOARM transmission electron microscope equipped with a cold field-emission gun and spherical-aberration correctors, operated at an accelerating voltage of 200 kV. TEM specimens were prepared by dispersing the catalyst powder in 2-propanol through ultrasonication and drop-casting the suspension onto holey carbon-coated Cu grids.

Surface chemical states were analyzed by X-ray photoelectron spectroscopy (XPS) with a PHI 5000 VersaProbe II, using a 45° take-off angle and a 100 μm X-ray spot. XPS spectra were calibrated by referencing the binding energies to the C 1 s signal at 284.8 eV.

Further analysis of the surface chemistry was performed by diffuse reflectance infrared Fourier transform spectroscopy (DRIFTS) using a Bruker Invenio S spectrometer equipped with a liquid N_2-cooled MCT detector and a Harrick Praying Mantis diffuse reflectance accessory. Spectra were collected directly from the catalyst powders at a spectral resolution of 2 cm^{-1} by averaging 64 scans.

2.3. Catalytic activity tests and TPO

Catalytic activity for methane oxidation was evaluated in a fixed-bed reactor. In a typical test, a quartz U-tube reactor (inner diameter: 4 mm) was loaded with 50 mg of catalyst powder, supported on quartz wool. A PID-controlled furnace was employed to heat the reactor, with the temperature being monitored by a thermocouple located close to the catalyst bed. The reactor was fed with a gaseous mixture containing 0.3% CH_4 and 1.2% O_2 in N_2, at a total flowrate of 100 mL min^{-1} (corresponding to a gas hourly space velocity of 70000–180000 h^{-1}, depending on the catalyst bulk density). The outlet concentrations of CH_4, CO, CO_2, and O_2 were monitored continuously using an ABB AO2020 analyzer.

The experimental sequence followed during the catalytic tests is schematically reported in Fig. 1. First of all, while flowing the reaction mixture, the sample was pretreated at 100 °C for 30 min to remove physisorbed water, then it was heated up to 900 °C with a 10 °C min^{-1} ramp, followed by cooling to 300 °C. Since stabilization of the material can occur during this first reaction cycle, a second heating-cooling cycle between 300 and 900 °C was performed, taken as representative for the activity of the fresh sample. Afterwards, the catalyst was heated to 500 °C and, once the temperature stabilized, 20 ppm of SO_2 were added to the reaction mixture. A common temperature of 500 °C was selected for the sulfation tests in order to compare all catalysts under identical reaction conditions, despite at different methane conversion, to avoid the effects induced by temperature difference on sulfur adsorption, sulfate stability, or Pd/PdO redox behavior. The reactor was kept in stationary conditions for a 6 h time-on-stream (TOS) stage, then SO_2 was removed from the feed and the sample was cooled down. Finally, two further heating and cooling cycles between 300 and 900 °C were carried out, to observe the catalyst behavior after sulfation (3rd cycle) and after subsequent high-temperature exposure of the sulfated sample (4th cycle). Each test was repeated multiple times to prepare two different exhausted samples (Fig. 1): a first "post-TOS" sample was obtained after the TOS stage, and a second "spent" sample was recovered at the end of the 4th cycle. Methane oxidation tests were also carried out in wet conditions, adding 5% H_2O to the inlet mixture using a Bronkhorst Controlled Evaporation and Mixing (CEM) apparatus and a heated gas line.

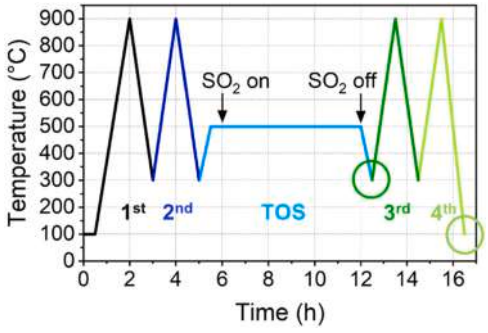


Fig. 1. Scheme of the procedure followed for performing the catalytic tests, including four heating-cooling cycles and a time-on-stream (TOS) stage in the presence of SO_2. Two exhausted samples were recovered, after the TOS stage ("post-TOS" sample, dark green circle) and at the end ("spent" sample, light green circle).

The same experimental set-up was also used to carry out temperature-programmed oxidation (TPO) experiments, to monitor how the PdO-Pd transition at high temperature was affected by SO_2 poisoning. The fixed-bed reactor was loaded with 50 mg of catalyst and was subjected to a heating and cooling cycle up to 900 °C (10 °C min^{-1} ramp), under 50 mL min^{-1} flow of 0.3% CH_4 and 1.2% O_2 in N_2 (i.e., the reacting mixture), which worked as pretreatment/activation step. Afterwards, the reactor was fed with 1.2% O_2 in N_2 (50 mL min^{-1}) and other two heating-cooling cycles between 200 and 900 °C (10 °C min^{-1}) were performed, to investigate the PdO/Pd redox behavior in the fresh catalyst by monitoring the O_2 concentration in the outlet (the 2nd cycle was taken as representative). Subsequently, a TOS stage was performed by keeping the sample at 500 °C for 6 h under a gas flow containing 20 ppm SO_2, 0.3% CH_4, and 1.2% O_2 in N_2 (50 mL min^{-1}), then SO_2 was removed from the feed and the sample was cooled down. Finally, three further heating and cooling TPO cycles (3rd – 5th) between 300 and 900 °C were carried out in a flow of 1.2% O_2 in N_2 (50 mL min^{-1}), to observe the catalyst redox behavior after sulfation. The whole procedure was performed on both the bare supports and the Pd-loaded catalysts, allowing the specific contribution of palladium to be reliably identified by difference (an example is reported in Fig. S1) [34]. This approach could not be applied to the Pd/Pr100 sample, however, since no distinct PdO reduction peaks could be identified. The calculation method used to quantify oxygen release and uptake from the TPO profiles is described in the Supplementary Material.

3. Results and discussion

3.1. Properties of the fresh catalysts

The main structural properties of the ceria/praseodymia supports are summarized in the Supporting Information file. Hydrothermal synthesis led to the formation of nanostructured materials, exhibiting faceted particles with low specific surface area within the 5 – 15 m^2 g^{-1} range (Table S1). Ce100 and Ce90Pr10 are characterized by nanocubes, Ce50Pr50 contains both cubic and rod-like particles, whereas Pr100 shows a fibrous morphology (Fig. S2). Notably, morphology was not independently varied within this series: all supports were prepared under identical hydrothermal conditions, and the observed morphological evolution resulted from the change in Ce/Pr composition. The two mixed oxides are solid solution of ceria and praseodymia, exhibiting a single set of XRD peaks characteristic of the fluorite structure typical of these materials (Fig. S3) [36,37].

Table 1 reports the main properties of the four fresh catalysts obtained after Pd impregnation. The Pd loading is similar in all samples, although slightly lower than the nominal value. The Pr content in the mixed oxides closely matches the nominal composition. After impregnation and calcination at 900 °C, the specific surface area decreases to the 3 – 6 m^2 g^{-1} range, likely due to thermally induced sintering of the

Table 1
Composition and structural properties of the fresh Pd catalysts.

Catalyst	Pd content[a] (wt%)	Pr content[b] (at%)	D_C[c] (nm)	SSA[d] ($m^2\ g^{-1}$)	D/F_{2g}[e]
Pd/Ce100	1.68	-	258	2.9	0.04
Pd/Ce90Pr10	1.65	10.6	153	4.3	1.54
Pd/Ce50Pr50	1.68	51.8	38	5.1	2.05
Pd/Pr100	1.57	-	60	6.1	-

[a] The Pd loading was measured via ICP-MS.
[b] The Pr content was evaluated via FESEM-EDX.
[c] The average crystallite size (D_C) of ceria was estimated using XRD data.
[d] The specific surface area (SSA) was measured using N_2-physisorption.
[e] Ratio between the areas of the D and F_{2g} Raman bands.

oxide particles. Given the intrinsically low surface area of these nanostructured supports, extensive Pd trapping through collapse of a developed porous structure is not expected to represent the dominant phenomenon. Nevertheless, the high-temperature treatment may promote partial incorporation of Pd species into the oxide surface and strengthen Pd-support interactions [34]. After calcination, the morphology of the supports is largely preserved, with only some minor changes (Fig. 2): nanocubes in the Pd/Ce100 and Pd/Ce90Pr10 samples are characterized by rounder edges and vertices, while shorter rods and fibers are present in Pd/Ce50Pr50 and Pd/Pr100. STEM-EDX maps were collected to evaluate the elemental distribution in the impregnated catalysts: large Pd particles of ~100 nm were detected in Pd/Ce100 and Pd/Ce90Pr10 (Fig. 2E, Fig. S4 and S5), while a finer Pd distribution was observed for Pd/Ce50Pr50 and Pd/Pr100 (Fig. 2F, Fig. S6 and S7), likely due to the stronger interaction between Pd and Pr [34].

XRD patterns confirm the presence of a single set of fluorite peaks for all the samples, indicating that the Ce-Pr solid solution remains unaltered (Fig. 3A). However, additional phases were detected too (Fig. 3B). The main PdO peak around 34° was observed in the Pd/Ce100 and Pd/Ce90Pr10 samples, signaling the presence of PdO nanoparticles [38]. Moreover, three peaks appeared in the 31° – 35° range for Pd/Pr100, attributable to the formation of a Pd-Pr-O_x mixed oxide during calcination at high temperature [34,39]. The average size of the ceria crystallites decreases with increasing Pr content, in agreement with previous studies [34], reaching a minimum in Pd/Ce50Pr50, in line with the trend in specific surface area (Table 1).

Consistent findings were provided by Raman spectroscopy (Fig. 3C). The three Ce-containing samples show an intense F_{2g} peak in the Raman spectra, corresponding to the Ce-O_8 symmetric breathing mode typical of the ceria fluorite structure [41,42]. This component is located at 464 cm^{-1} for Pd/Ce100, while it red-shifts to 460 cm^{-1} for Pd/Ce90Pr10 and down to 445 cm^{-1} for Pd/Ce50Pr50, signaling increasing structural distortion induced by Pr incorporation into the ceria lattice [43,44], likely arising from the slight ionic size mismatch between Ce^{4+} and Pr^{3+}/Pr^{4+} [45]. At the same time, a D band linked to the presence of structural defects can be detected around 570 cm^{-1}; this signal is rather weak for Pd/Ce100 but much more pronounced in Pr-doped ceria. The higher ratio between the areas of the D and F_{2g} bands (D/F_{2g}, Table 1) points to an increased defectiveness upon Pr addition, mainly due to the formation of charge-compensating oxygen vacancies (550 – 570 cm^{-1}) and anionic Frenkel sites (ca. 595 cm^{-1}) [42,46], likely associated with the higher reducibility of Pr compared to Ce [41]. Nevertheless, the strong increase in the D/F_{2g} ratio can also be partially caused by other effects, such as the Raman resonance of specific Pr^{4+}-containing sites exhibiting an enhanced signal at 570 cm^{-1} [47], or the lower light penetration depth in the Pr-doped samples, which confines the analysis to surface regions that are naturally enriched in defects [48]. Therefore, the D/F_{2g} values reported herein should be only considered as semi-quantitative indicators to monitor the relative structural evolution of each catalyst upon treatment. In agreement with

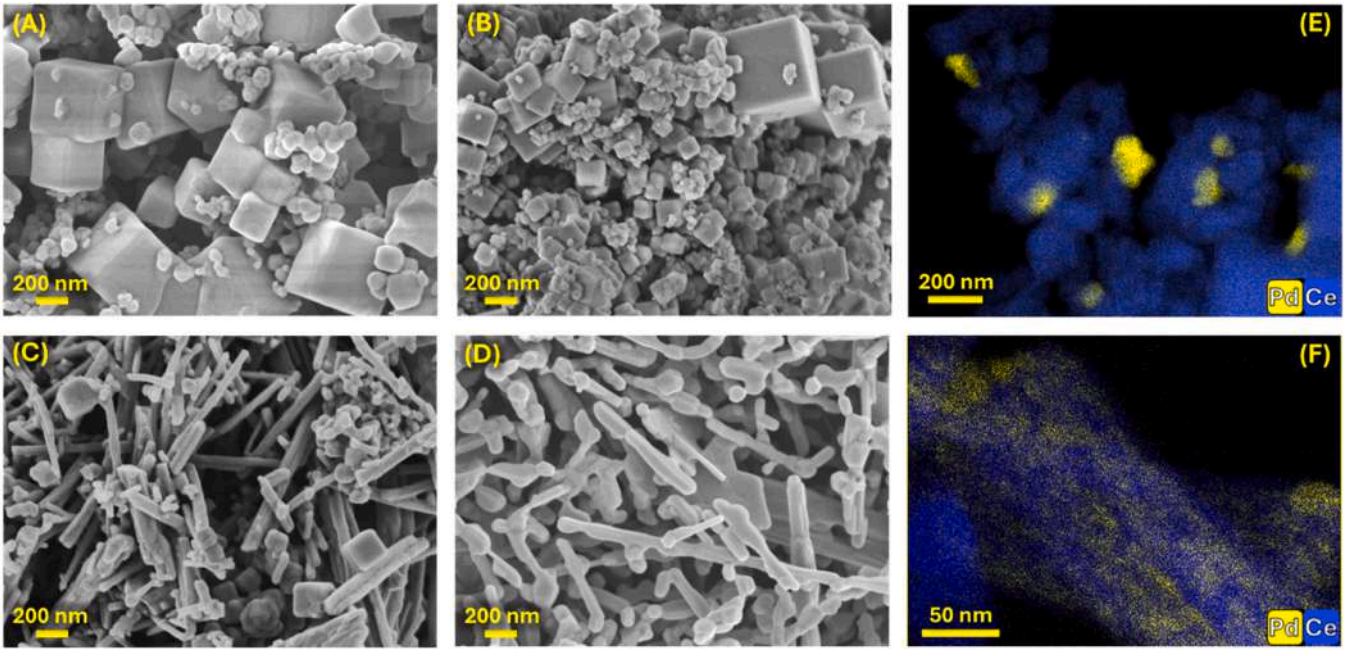


Fig. 2. FESEM micrographs of the fresh Pd-based catalysts: Pd/Ce100 (A), Pd/Ce90Pr10 (B), Pd/Ce50Pr50 (C), and Pd/Pr100 (D); STEM-EDX maps of the fresh Pd/Ce100 (E) and Pd/Ce50Pr50 (F).

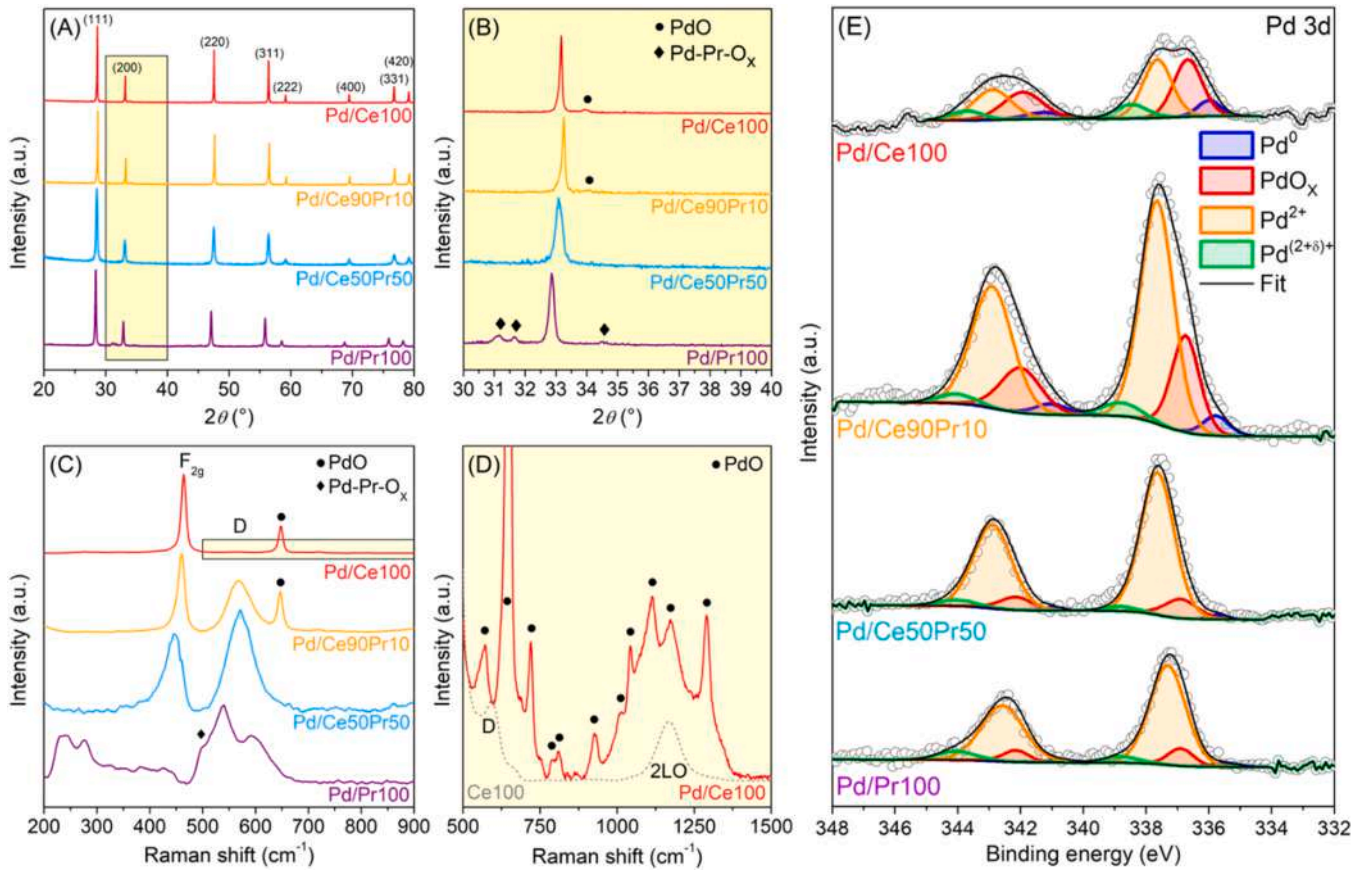


Fig. 3. X-ray diffractograms of the fresh Pd-based catalysts (A), with a magnification of the 30° – 40° range showing the secondary phases (B). Normalized Raman spectra of the four fresh catalysts (C), with a magnification showing all the PdO signals in the spectrum of Pd/Ce100 (D) together with the Raman profile of the Ce100 support (grey dashed line) for comparison [40]. Deconvolved high-resolution XPS spectra of the fresh Pd-based catalysts in the Pd 3d core level (E).

XRD results, signals associated with Pd-based phases were also detected in the Raman spectra of the fresh catalysts. Pd/Ce100 and Pd/Ce90Pr10 exhibited a distinct peak at 647 cm^{-1}, that can be assigned to the B_{1g} mode of PdO [46], as well as other weaker PdO-related vibrational features (enlarged in Fig. 3D). A band at 500 cm^{-1} in the Pd/Pr100 spectrum is instead related to the formation of the Pd-Pr-O_x mixed oxide [34]. This may decrease the fraction of readily accessible PdO species and hinder the catalytic activity of the latter sample.

The Pd chemical state at the surface of the fresh catalysts was investigated via XPS. By deconvolving the high-resolution spectra of the Pd 3d core level (Fig. 3E), four pairs of peaks were identified, corresponding to different palladium species. Focusing on the Pd $3d_{5/2}$ level, the characteristic signal of metallic palladium (Pd^0) was detected at 335.9 eV, while that associated with Pd^{2+} species (e.g., in segregated PdO domains) appeared at 337.6 eV [49,50]. An additional component at an intermediate binding energy (ca. 336.7 eV) indicated the presence of palladium species with an oxidation state between 0 and +2 (PdO_x) [50]. According to previous studies, these species may form at the interface between PdO and metallic Pd or after oxygen chemisorption on metallic Pd, and can play a crucial role for palladium oxidation and decomposition [49]. Finally, a high-binding-energy component at 338.5 eV was assigned to highly oxidized palladium species ($Pd^{(2+\delta)+}$) [51], which typically arise by the incorporation of palladium ions into the surface layers of the support, forming a solid solution with the host lattice [46]. As shown in Table 2, the relative abundance of reduced species (Pd^0 and PdO_x) markedly decreases with increasing praseodymium content, while Pd^{2+} becomes dominant. These results confirm that Pr incorporation into the ceria lattice promotes the stabilization of palladium in higher oxidation states, in line with previous studies [33–35].

Table 2
Relative abundance of palladium chemical species at the surface of the fresh catalysts resulting from deconvolution of the Pd 3d XPS spectra.

Catalyst	Palladium species (at%)			
	Pd^0	PdO_x	PdO	$Pd^{(2+\delta)+}$
Pd/Ce100	8.7	39.2	41.2	10.9
Pd/Ce90Pr10	6.3	32.7	55.2	5.8
Pd/Ce50Pr50	1.4	11.0	83.7	3.9
Pd/Pr100	2.2	10.1	80.2	7.5

3.2. Catalytic activity and sulfur poisoning

The catalytic activity and sulfur tolerance of the four synthesized catalysts were assessed by performing methane oxidation tests in dry conditions according to the scheme reported in Fig. 1. In this procedure, the second heating/cooling cycle can be considered representative of the catalytic performance of the fresh materials.

The light-off curves reported in Fig. 4 demonstrate the significant influence of Pr addition on the CH_4 oxidation activity of Pd/ceria catalysts. Pd/Ce100 and Pd/Ce90Pr10 exhibit higher activity, reaching full conversion within 600 °C. During the cooling run, however, a loss of activity was observed below 850 °C; this indicates that PdO has undergone thermal decomposition to metallic Pd during heating, which is a less active phase towards methane oxidation. The activity was then recovered thanks to Pd reoxidation to PdO, occurring in the 700 – 650 °C range. Pd/Ce50Pr50 and Pd/Pr100 exhibited lower activity but showed no significant hysteresis between the heating and cooling profiles, which means a much lower extent of PdO decomposition or Pd reoxidation.

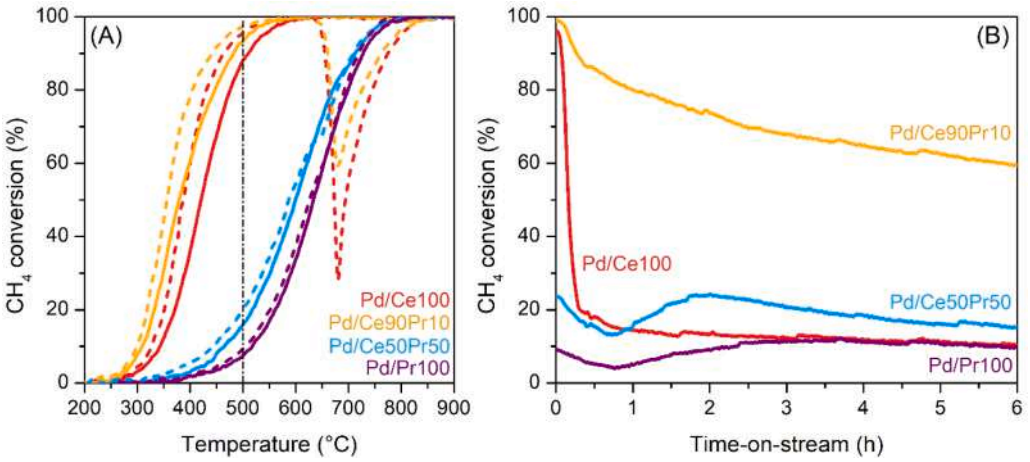


Fig. 4. Methane oxidation light-off curves of the fresh Pd-based catalysts (A), showing CH_4 conversion during the second heating (solid lines) and cooling (dashed lines) cycle (feed: 0.3% CH_4 + 1.2% O_2 in N_2). Evolution of CH_4 conversion over time during the TOS stage (B), performed at 500 °C in the presence of 20 ppm of SO_2 added to the reaction mixture.

Previous studies have attributed this effect to the stabilization of Pd in higher oxidation states in the presence of Pr [33,34], as confirmed by the XPS results (Table 2). At low temperatures, catalysts containing both reduced and oxidized Pd species generally exhibit higher activity, while PdO represents the most active phase at high temperatures [12,17,52]. Here, the Pd/Ce90Pr10 sample showed the best overall activity, possibly due to a favorable balance between reduced and oxidized Pd species. Specifically, it showed higher activity than Pd/Ce100 at low temperatures and higher stability at high temperatures, being less affected by PdO decomposition, as evidenced during the cooling phase. The lower activity of the Pd/Ce50Pr50 and Pd/Pr100 samples might instead be caused by an excessively strong Pd-support interaction with the increase in Pr content.

Fig. 4B shows the evolution of methane conversion over time during the TOS stage, which was performed in stationary conditions at 500 °C. At this temperature, Pd/Ce100 and Pd/Ce90Pr10 reached almost complete CH_4 oxidation, but their activity started to decrease upon the introduction of SO_2 (20 ppm) into the reaction mixture. In 30 min, the methane conversion over Pd/Ce100 dropped from 96% to 18%, followed by a slower decrease down to 10% after 6 h. Pd/Ce90Pr10 exhibited a much better tolerance to the presence of sulfur, with a slower decrease in activity and a retained methane conversion of 80% after 1 h and 60% after 6 h of testing. The higher stability of this sample is also confirmed by a comparison of the methane oxidation rate over the test (see Table S2).

To determine whether the residual CH_4 conversion measured after sulfur exposure could be associated with the intrinsic activity of the ceria-based supports after complete Pd deactivation, methane oxidation was also tested over the bare supports. At 500 °C in dry conditions, Ce100 showed negligible CH_4 conversion, whereas Ce90Pr10 remained below 5% (see Fig. S8). These conversion values are substantially lower than those measured for the corresponding Pd-containing catalysts after 6 h of SO_2 exposure. This suggests that, despite the progressive deactivation, these catalysts retained moderate Pd-related activity at the end of the TOS.

A different behavior was observed in the case of high Pr loading. Both Pd/Ce50Pr50 and Pd/Pr100 showed a slight decrease in activity, which however was limited to the first 45 min of exposure to SO_2. After this time, the methane conversion started to increase, returning temporarily to the initial value. The activity then started to slowly decrease in the last four hours of TOS. Throughout the whole TOS stage, methane conversion decreased from 24% to 15% for Pd/Ce50Pr50, while it did not change significantly for Pd/Pr100, remaining at 10% after 6 h.

It should also be considered that the different support morphologies may contribute to the observed sulfur-poisoning behavior. Indeed, the interaction of SO_2 with ceria is known to depend on the exposed crystallographic facets, surface reducibility, and defect density. Tumuluri et al. reported a clear structure-sensitive dependence of SO_2 adsorption on CeO_2 nanocrystals: in their study, sulfate formation followed the order rods > cubes > octahedra, with more defective and reducible rod-like ceria showing stronger interaction with sulfur species [53]. Ceria morphology can also influence Pd dispersion, oxidation state, and metal-support interactions, thereby affecting methane oxidation activity [54]. Nevertheless, Pd/Ce100 and Pd/Ce90Pr10 exhibit a very similar nanocubic morphology and comparable Pd particle size, while showing markedly different responses to SO_2 exposure. This comparison therefore supports a significant role of Pr incorporation itself in modifying sulfur-catalyst interactions. For the Pr-rich catalysts, however, a contribution of the different nanoshape to the observed behavior cannot be completely excluded.

Two heating/cooling cycles of methane oxidation were then performed over the catalysts exposed to SO_2 during the TOS. Comparisons between the light-off curves and reaction rates measured before (2^{nd} cycle) and after TOS (3^{rd} and 4^{th} cycles) are reported in Fig. 5. Pd/Ce100 exhibited lower activity during the 3^{rd} heating run with respect to the 2^{nd} one, with a light-off curve shifted to ~100 °C higher temperature due to sulfur poisoning. However, the profile of the 3^{rd} cooling run is very similar to that of the 2^{nd}, and the 4^{th} cycle closely matches the 2^{nd} one, despite a certain loss of activity due to PdO decomposition during heating at 750 – 800 °C.

A similar behavior was observed for Pd/Ce90Pr10 as well (Fig. 5B): SO_2 poisoning caused a shift of the conversion curve of the 3^{rd} heating run (ca. +90 °C with respect to the 2^{nd} cycle), which was fully reversible after reaching high temperatures. Indeed, the 3^{rd} and 4^{th} cooling profiles perfectly overlap with the 2^{nd} one, while the activity during the 4^{th} heating run was even slightly higher than that of the fresh sample (Fig. 5E). This suggests that the sulfated compounds deposited on the Ce-rich catalysts can be almost entirely removed at high temperature, enabling effective regeneration. Overall, as shown in Fig. 5F, the Pd/Ce90Pr10 sample maintains its leading performance among the analyzed set of catalysts.

A completely different behavior was noticed for the two Pr-rich materials. Their initial activity up to 500 °C was almost unaltered after the TOS stage, while at higher temperatures significant changes were observed. During the 3^{rd} heating run, the conversion of the Pd/Ce50Pr50 catalyst dropped significantly from 640 to 730 °C (Fig. 5C), signaling PdO reduction. This was followed by an increase in

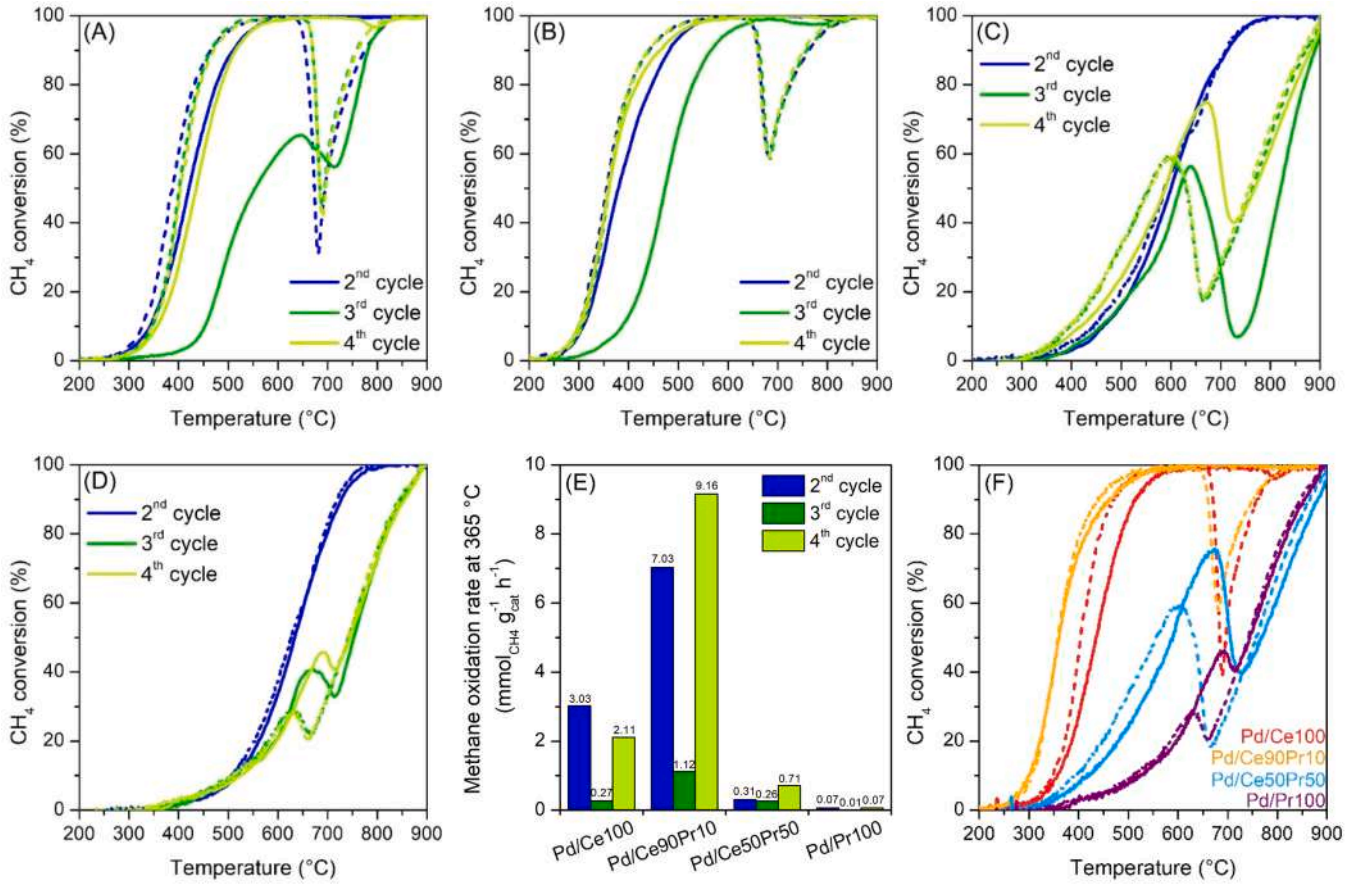


Fig. 5. Methane conversion curves as a function of temperature during heating (solid lines) and cooling (dashed lines) of the 2nd, 3rd, and 4th cycles of methane oxidation (feed: 0.3% CH_4 + 1.2% O_2 in N_2) over Pd/Ce100 (A), Pd/Ce90Pr10 (B), Pd/Ce50Pr50 (C), and Pd/Pr100 (D). Evolution of the specific reaction rate of methane oxidation at 365 °C through the three heating cycles (E). Comparison of the conversion curves of the four catalysts during the 4th heating (solid lines) and cooling (dashed lines) cycle (F).

conversion, though complete methane oxidation was no longer achieved during the test (with a maximum conversion of 94% at 900 °C). A marked Pd-PdO transition was also visible during cooling, with Pd reoxidation occurring in the 650 – 600 °C range. The situation was slightly improved during the 4th heating run. The low-temperature activity seemed slightly higher than that of the fresh material in the 2nd cycle, but a marked decrease in conversion due to PdO decomposition was still visible in the 670 – 730 °C range. The 4th cooling profile overlapped with the 3rd one, suggesting that the catalyst performance had already stabilized after the 3rd heating/cooling cycle. This suggests that exposure to SO_2 strongly weakens the Pd-support interactions in the Pd/Ce50Pr50 material, thereby promoting PdO decomposition during heating. Regeneration at high temperatures only partially mitigated these effects.

The Pd/Pr100 sample exhibited an analogous behavior (Fig. 5D), with a low-temperature activity not significantly influenced by sulfur exposure, though this negatively impacted its high-temperature performance. Signs of PdO reduction were observed between 670 and 710 °C during the 3rd and 4th heating runs, while Pd reoxidation occurred at 660 – 630 °C during cooling. The conversion curves of the 3rd and 4th cycles showed very similar profiles, indicating that exposure at high temperature after the TOS had a very limited impact on the activity. Again, sulfur seemed to irreversibly affect the Pd-Pr interaction.

Since the palladium redox cycle seemed to be strongly influenced by sulfur, TPO experiments were performed before and after a TOS stage in the presence of SO_2. The resulting profiles are displayed in Fig. S9, while the quantity of oxygen released during heating is reported in Table 3. This high-temperature oxygen release is mainly associated with PdO decomposition, although a partial contribution from sulfate decomposition cannot be excluded. In general, the addition of Pr strongly reduces the amount of palladium taking part in reduction and reoxidation, since the stronger Pd-Pr interaction keeps the noble metal in a more oxidized state and hinders its reduction at high temperature [34]. Concerning the effect of sulfation, Pd/Ce100 and Pd/Ce90Pr10 exhibited a slight increase in the amount of oxygen released after the TOS (i.e., in the 3rd cycle); however, this effect was significantly mitigated in the two following cycles (4th and 5th). Instead, the Pd/Ce50Pr50 sample showed a marked relative increase in the fraction of PdO reduced at high temperature, consistent with the loss of activity observed during the catalytic tests. These outcomes further support the claim that exposure to SO_2 weakens the Pd-support interactions, promoting PdO reduction during heating. This effect is particularly pronounced and non-reversible for the Pd/Ce50Pr50 material.

Table 3
Quantity of oxygen released due to PdO decomposition during heating in TPO experiments, before (2nd cycle) and after (3rd – 5th cycles) exposure to SO_2. The relative increase with respect to the 2nd cycle is reported in brackets.

Catalyst	Released oxygen ($\mu mol_{O2}\ g_{cat}^{-1}$)			
	2nd cycle	3rd cycle	4th cycle	5th cycle
Pd/Ce100	68	76 (+12%)	78 (+15%)	73 (+7%)
Pd/Ce90Pr10	55	65 (+18%)	59 (+7%)	58 (+5%)
Pd/Ce50Pr50	1.9	3.5 (+84%)	3.1 (+63%)	2.5 (+32%)

3.3. Investigation of exhausted catalysts

In order to better investigate the role of sulfur in the catalyst deactivation mechanisms, two representative exhausted samples were prepared for each material (as shown in Fig. 1) and thoroughly analyzed. A "post-TOS" sample was collected after the TOS stage, to understand how the structural and chemical properties of the catalyst change after exposure to SO_2. The "spent" sample recovered at the end of the 4^{th} cycle was instead studied to evaluate the effect of repeated exposure to high temperatures. Both samples were obtained after tests performed in dry conditions.

Two techniques were used to determine the composition of the exhausted samples and to verify the presence of sulfur. FESEM-EDX was employed to obtain information about the bulk composition, since its penetration depth is greater than the size of the catalyst particles. The surface chemical composition was instead investigated via XPS. The resulting sulfur content values (wt%) are reported in Table 4.

The presence of sulfur was detected in all the post-TOS samples, especially at the catalyst surface. The high-resolution XPS spectra of the S 2p core level (Fig. 6) feature a single S $2p_{3/2}$ peak at a binding energy of 169.2 – 168.7 eV, with a shoulder corresponding to the S $2p_{1/2}$ line at 170.4 – 169.9 eV (spin-orbital splitting of ca. 1.2 eV). This signal can be attributed to sulfur in a +6 valence state, indicating the formation of sulfate species (SO_4^{2-}) on the catalyst surface [32,55]. Interestingly, the sulfur quantity strongly depends on the support composition, increasing remarkably with the Pr content. The spent samples generally contain a lower sulfur amount, indicating that the S-containing species undergo thermal decomposition and desorption during high-temperature operation. In particular, almost no traces of sulfur were detected in the Pd/Ce100 and Pd/Ce90Pr10 spent samples, confirming that these catalysts can be effectively regenerated through high-temperature treatment. In contrast, S species were only partially removed from the Pd/Ce50Pr50 catalyst, as evidenced by the substantial S residues still present in the spent material (Table 4). Interestingly, Pd/Pr100 showed a decrease in surface sulfur species but a slight increase in the bulk sulfur content determined by EDX. This suggests that, rather than being extensively removed, sulfur-containing species undergo redistribution and reorganization within the latter catalyst during high-temperature treatment.

Further insights into the surface chemical state were obtained from the high-resolution XPS spectra of O 1 s, Ce 3d, Pr 3d, and Pd 3d core levels. The quantitative results derived from spectral deconvolution of the fresh, post-TOS, and spent catalysts are summarized in Table 5.

Analysis of the O 1 s core level revealed two main components for all the catalysts (Fig. S10). The low-binding-energy peak at approximately 529 eV can be attributed to lattice oxygen (O_{latt}), while the higher-binding-energy contribution in the 531.5–532.5 eV range corresponds to surface capping oxygen species (O_{capp}), including adsorbed hydroxyl groups, carbonates, and other oxygen-containing adventitious organic species [56–59]. Sulfation induced a marked increase in the relative abundance of the O_{capp} species for Pd/Ce50Pr50 and Pd/Pr100 (Table 5), attributable to the formation of SO_4^{2-} species [32]. These sulfates are then only partially desorbed in the spent samples, consistently with the persistence of the S 2p signal (Fig. 6).

Deconvolution of the Ce 3d XPS spectra was carried out using a total of ten components, to take into account spin-orbit coupling and multiplet splitting [60,61]: six associated with Ce^{4+} species and four attributed to Ce^{3+} ions (Fig. S11). A similar fitting strategy was adopted for the Pr 3d core level (Fig. S12), which was also modeled using ten components, with six peaks assigned to Pr^{4+} species and four to Pr^{3+} ions [62]. Sulfur exposure led to partial reduction of the Ce-Pr oxide matrix, as evidenced by the increased relative fractions of Ce^{3+} and Pr^{3+} in the post-TOS samples (Table 5). This reduction is likely coupled with the oxidation of SO_2 to sulfate species during surface sulfation [55] and is more pronounced for the Pr-rich catalysts. Following high-temperature regeneration, the concentration of reduced species returned to values comparable to those of the fresh catalysts, with the exception of Pd/Pr100, for which re-oxidation of Pr remained incomplete.

Regarding palladium (Fig. 6 E-H), a general increase in reduced Pd species (Pd^0 and PdO_x) was observed in both the post-TOS and spent catalysts, indicating that sulfur exposure weakens the Pd-support interaction and that this effect is not fully reversed upon thermal regeneration. Such modulation of the metal-support interaction, resulting in a higher proportion of reduced Pd, can be the reason for the enhanced methane oxidation rate of the spent Pd/Ce90Pr10 and Pd/Ce50Pr50 at low temperatures (Fig. 5E), where the coexistence of metallic Pd and PdO is associated with improved activity [52]. In this context, partial Pd reduction can be regarded as an additional optimization of the balance between reduced and oxidized Pd species in Pd/Ce90Pr10, contributing to the better catalytic performance.

Concerning catalyst morphology, FESEM imaging did not evidence major alterations in the post-TOS and spent Pd/Ce100 and Pd/Ce90Pr10 catalysts (Fig. S13), apart from a slight rounding of the smaller nanocubes, likely induced by repeated exposure to high temperatures. More evident morphological modifications were detected for the Pr-rich catalysts, which exhibited shorter and more rounded nanorods that in some cases appeared partially fused together, again due to thermal effects.

To gain deeper insight into sulfur distribution in the exhausted catalysts, an extensive STEM-EDX investigation was performed. Representative EDX maps collected on the post-TOS samples are reported in Fig. 7. Palladium dispersion did not show significant variations compared to the fresh catalysts: Pd was found in relatively large particles (~100 nm) dispersed within the nanocubic ceria matrix for Pd/Ce100 and Pd/Ce90Pr10, whereas it was more finely and homogeneously distributed over the nanorods of Pd/Ce50Pr50. A slight sintering with the formation of larger aggregates was observed only for Pd/Pr100.

EDX elemental mapping was particularly informative for elucidating sulfur localization. In Pd/Ce100 (Fig. 7A), sulfur was distributed throughout the sample. Notably, line-scan measurements across Pd nanoparticles revealed that the S signal, although weak due to the overall limited amount of deposited sulfates, closely correlated with the Pd intensity profile. This matching suggests that SO_2 preferentially interacts with palladium, leading to accumulation of sulfur-containing species in Pd-rich regions. This behavior is consistent with the possible presence of palladium sulfate-like species, whose formation has been previously detected via in situ IR spectroscopy [63] and supported by DFT studies [64]. The deposition of such species directly on the Pd particles would consequently cause poisoning of the active sites, accounting for the rapid deactivation of Pd/Ce100 observed during the TOS tests in the presence of SO_2 (Fig. 4B). This behavior is also consistent with the more pronounced reduction of Pd relative to Ce revealed by XPS, due to preferential sulfation of PdO (Table 5).

A different behavior was observed for Pd/Ce90Pr10 (Fig. 7B). Line-scan analyses showed that sulfur no longer followed the Pd distribution,

Table 4
Sulfur content in the post-TOS and spent Pd-based catalysts, calculated on a S/(Ce+Pr+O+Pd+S) basis by using FESEM-EDX data for bulk composition and XPS data for surface composition (n.d. = not detected). D/F_{2g} ratio of the fresh, post-TOS, and spent samples, calculated from the Raman spectra.

Catalyst	Bulk sulfur content (wt%)		Surface sulfur content (wt%)		Raman D/F_{2g} ratio		
	Post-TOS	Spent	Post-TOS	Spent	Fresh	Post-TOS	Spent
Pd/Ce100	0.03	0.01	1.1	n.d.	0.04	0.04	0.03
Pd/Ce90Pr10	0.04	n.d.	1.6	n.d.	1.54	1.39	1.47
Pd/Ce50Pr50	0.72	0.39	8.5	2.7	2.05	6.18	4.11
Pd/Pr100	1.36	1.91	11.7	9.1	n.d.	n.d.	n.d.

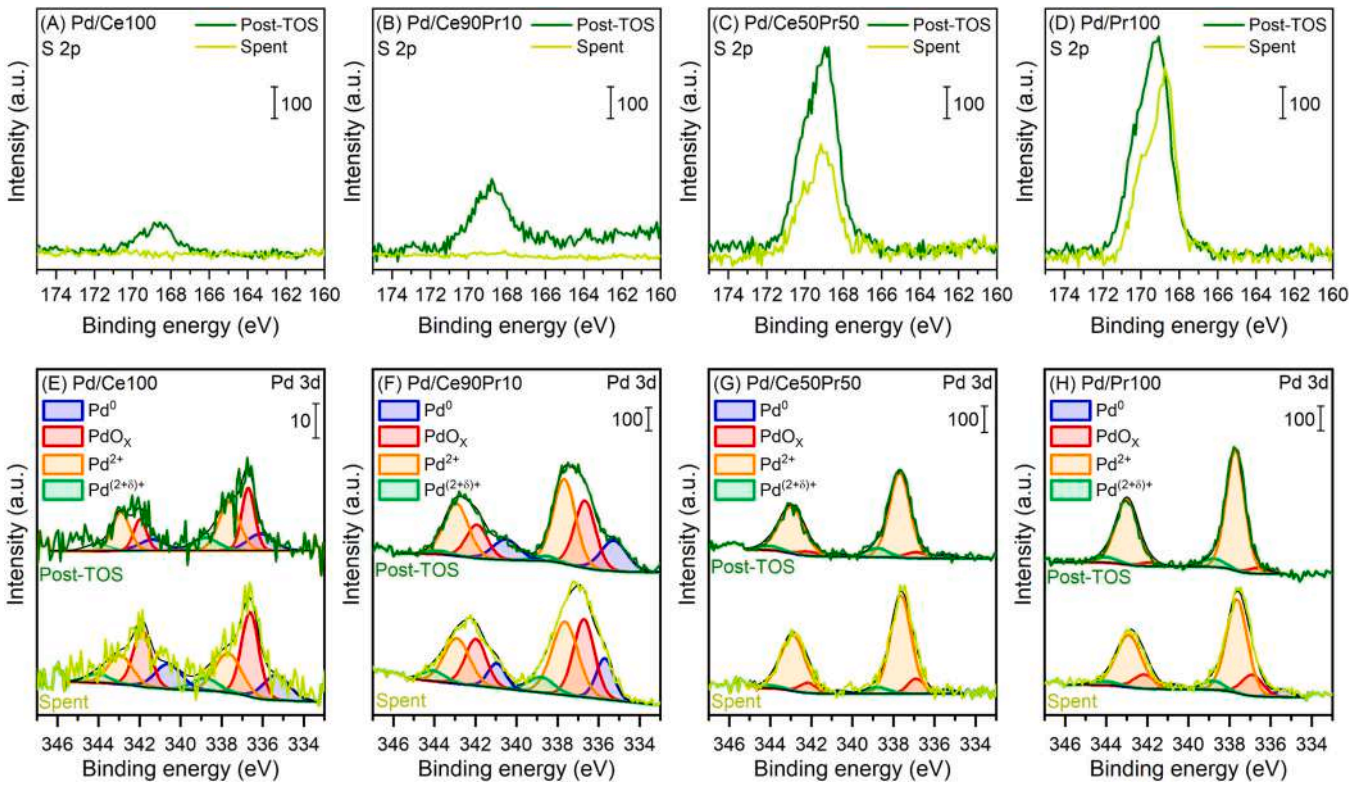


Fig. 6. High-resolution XPS spectra of the post-TOS and spent Pd-based catalysts in the S 2p core level for Pd/Ce100 (A), Pd/Ce90Pr10 (B), Pd/Ce50Pr50 (C), and Pd/Pr100 (D), and in the Pd 3d core level for Pd/Ce100 (E), Pd/Ce90Pr10 (F), Pd/Ce50Pr50 (G), and Pd/Pr100 (H).

Table 5
Relative abundance of oxygen, cerium, praseodymium, and palladium chemical species at the surface of the fresh, post-TOS, and spent catalysts resulting from deconvolution of the O 1 s, Ce 3d, Pr 3d, and Pd 3d XPS spectra.

Catalyst	Condition	O species (at%)		Ce species (at%)		Pr species (at%)		Pd species (at%)			
		O_{capp}	O_{latt}	Ce^{3+}	Ce^{4+}	Pr^{3+}	Pr^{4+}	Pd^{0}	PdO_x	Pd^{2+}	$Pd^{(2+\delta)+}$
Pd/Ce100	Fresh	49.3	50.7	24.0	76.0	-	-	8.7	39.2	41.2	10.9
	Post-TOS	50.4	49.6	26.5	73.5	-	-	17.8	29.4	40.5	12.3
	Spent	51.1	48.9	20.2	79.8	-	-	21.8	40.8	28.4	9.0
Pd/Ce90Pr10	Fresh	44.5	55.5	17.7	82.3	50.2	49.8	6.3	32.7	55.2	5.8
	Post-TOS	44.3	55.7	17.9	82.1	55.5	44.5	19.7	31.2	46.5	2.7
	Spent	47.8	52.2	16.3	83.7	50.8	49.2	15.4	35.0	41.0	8.6
Pd/Ce50Pr50	Fresh	45.2	54.8	12.8	87.2	62.1	37.9	1.4	11.0	83.7	3.9
	Post-TOS	75.4	24.6	24.0	76.0	67.8	32.2	3.3	6.0	82.2	8.5
	Spent	59.6	40.4	11.7	88.3	62.6	37.4	3.1	10.3	81.2	5.4
Pd/Pr100	Fresh	59.3	40.7	-	-	60.7	39.3	2.2	10.1	80.2	7.5
	Post-TOS	86.0	14.0	-	-	74.4	25.6	-	4.7	87.4	7.9
	Spent	72.8	27.2	-	-	69.6	30.4	4.8	16.3	72.5	6.4

but was more evenly distributed throughout the analyzed region, with a similar profile to those of Ce and Pr instead. Further quantitative EDX analysis performed in two distinct regions, one selected on the bare support (Area 1) and one including a Pd nanoparticle (Area 2), specifically revealed significantly different Pd contents but very similar sulfur concentrations, confirming that preferential sulfur deposition on Pd is avoided. Moreover, the Pr/(Ce+Pr) atomic ratio was comparable in both areas (around 0.11), in agreement with the nominal Pr content of the fresh catalyst (Table 1). In this sample, sulfates were evenly distributed across the material rather than selectively accumulated on the Pd phase, resulting in a reduced poisoning of the active sites, which can explain the mitigated deactivation rate observed during the TOS test (Fig. 4B).

As expected, a significantly higher sulfur signal was detected in the Pr-rich samples, reflecting their larger sulfate uptake after SO_2 exposure. In post-TOS Pd/Ce50Pr50, sulfur was preferentially localized at the particle surface, independently of Pd concentration. This is demonstrated by the comparison between Areas 1 and 2 in Fig. 7C, both characterized by a low Pd content (<1 wt%) wherein sulfur is approximately three times more abundant on the surface region (Area 1). Interestingly, these regions also exhibited a markedly different Pr/Ce ratio, which increases from ~0.8 to values above 2 moving towards the surface. Similar trends were observed when comparing Areas 3 and 4, which are characterized by higher Pd contents (~6 wt%): Area 4 close to the surface showed both a higher sulfur concentration and a higher Pr/Ce ratio (1.5) compared to Area 3 corresponding to an inner part of the material (Pr/Ce = 1.3). These findings indicate a surface enrichment in both Pr and sulfur, suggesting potential surface Pr segregation concurrently with sulfation. This behavior is consistent with the stronger affinity of Pr for sulfur evidenced throughout this study. The absence of a correlation between the sulfur and Pd distributions in Pd/Ce50Pr50 suggests weak poisoning of the active sites, in line with the good stability exhibited by this sample during the TOS test.

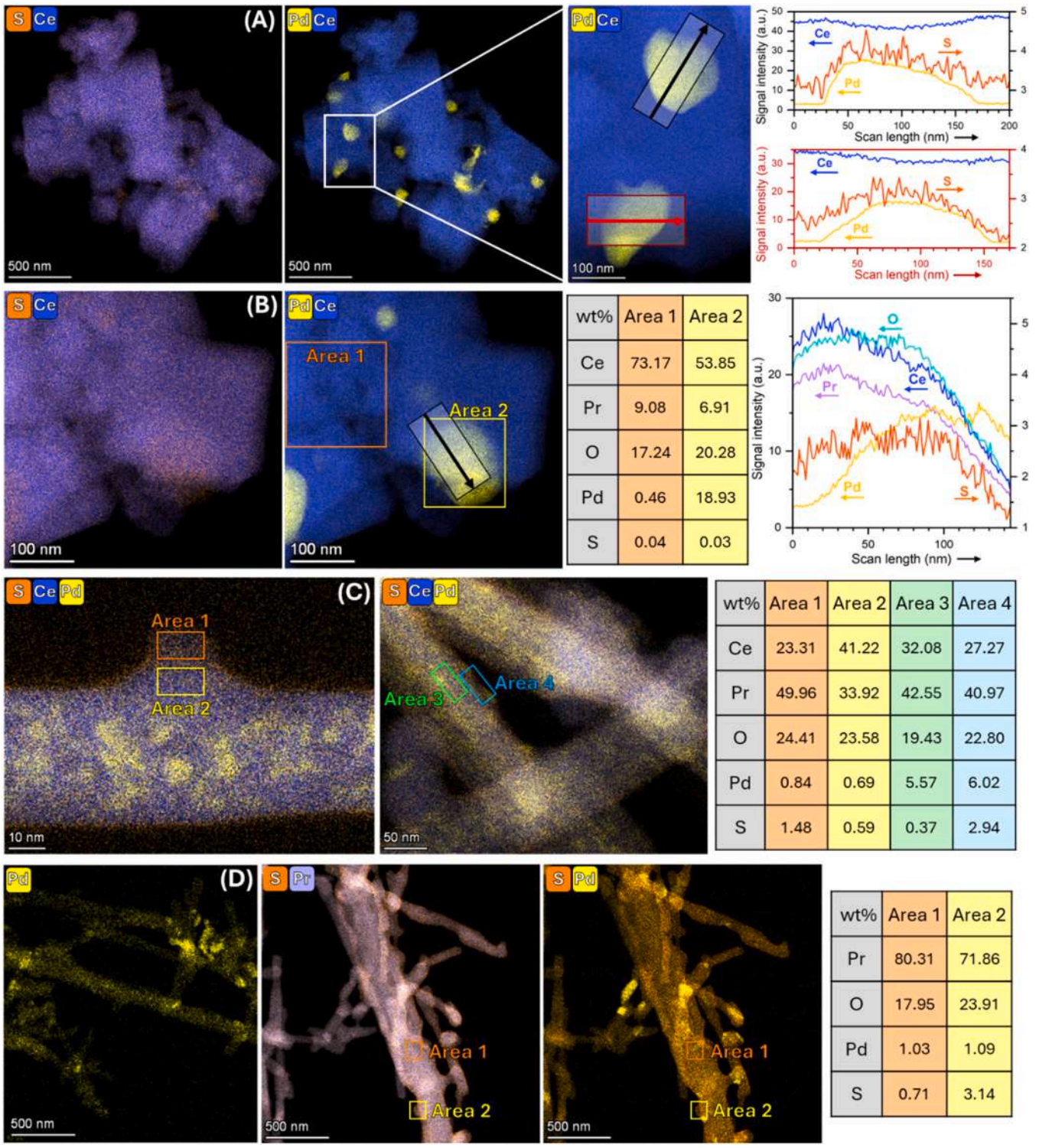
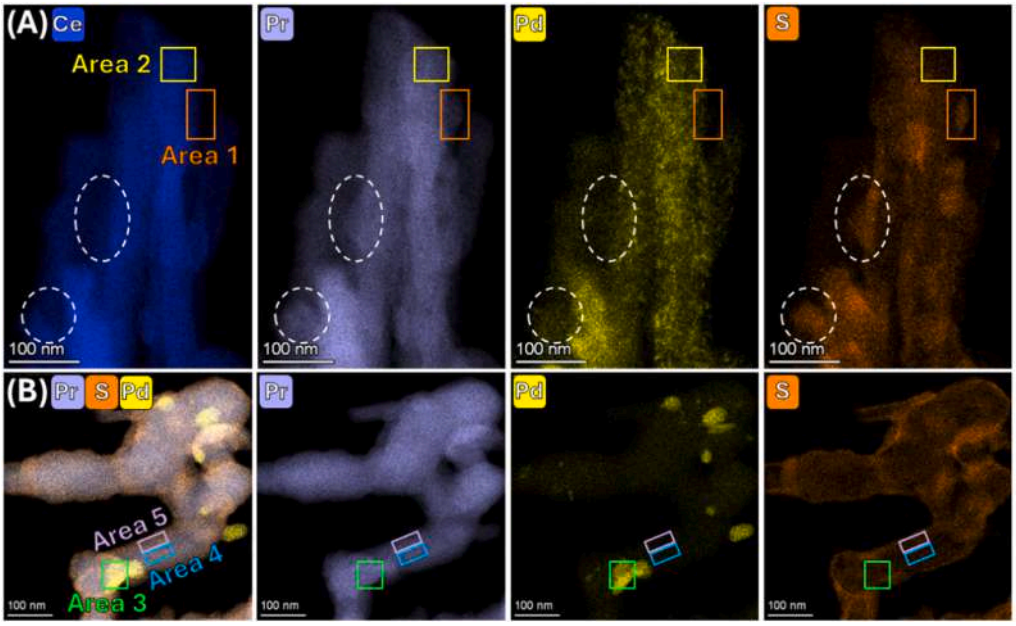


Fig. 7. STEM-EDX maps showing elemental distribution in the post-TOS samples: Pd/Ce100 (A), Pd/Ce90Pr10 (B), Pd/Ce50Pr50 (C), and Pd/Pr100 (D). In each line, the results of the microanalysis are also reported in the form of line scans or tables showing the elemental composition in selected areas (wt%).

Pd/Pr100 exhibited a similar preferential surface localization of sulfur, again independent of Pd content, as shown by the comparison of Areas 1 and 2 in Fig. 7D. In addition, partial Pd agglomeration was observed for this sample, resulting in the formation of larger Pd clusters after the catalytic runs and TOS in the presence of SO_2. This phenomenon can be attributed to the weakening of the Pd-support interaction when Pr reacts with SO_2. Therefore, the strong affinity between S and the praseodymia support, while effectively protecting Pd from poisoning, also promotes increased Pd mobility on the surface and consequent sintering.

STEM-EDX analysis was also carried out on the spent catalysts, as reported in Fig. 8. In line with the XPS results, sulfur was almost completely absent in spent Pd/Ce100 and Pd/Ce90Pr10, while a significant S amount was found in spent Pd/Ce50Pr50 and Pd/Pr100, confirming incomplete sulfate removal during high-temperature methane oxidation. In the latter samples, sulfur appeared less



wt%	Area 1	Area 2
Ce	5.76	21.29
Pr	46.78	37.50
O	39.13	39.04
Pd	1.62	2.00
S	6.71	0.18

wt%	Area 3	Area 4	Area 5
Pr	66.38	25.60	65.37
O	25.54	71.95	28.86
Pd	7.77	0.28	0.57
S	0.31	2.17	5.20

Fig. 8. STEM-EDX maps showing elemental distribution in the spent Pd/Ce50Pr50 (A) and Pd/Pr100 (B) samples. In each line, tables showing the elemental composition (wt%) in selected areas are also reported. The dashed circles highlight two S-containing aggregates in Pd/Ce50Pr50.

homogeneously distributed, coalescing instead into clustered regions, as evidenced by S EDX maps; this suggests the formation of bulk sulfate aggregates upon thermal treatment [65]. Again, no overlap between S and Pd signals was detected. Instead, the S-rich regions in Pd/Ce50Pr50 clearly overlapped with Pr-rich areas, as indicated by the dashed circles in Fig. 8A. Microanalysis revealed Pr/Ce ratios exceeding 8 in sulfur-rich regions (Area 1), representing much higher values than those measured in sulfur-poor regions (e.g., Pr/Ce was ~1.8 in Area 2). This indicates

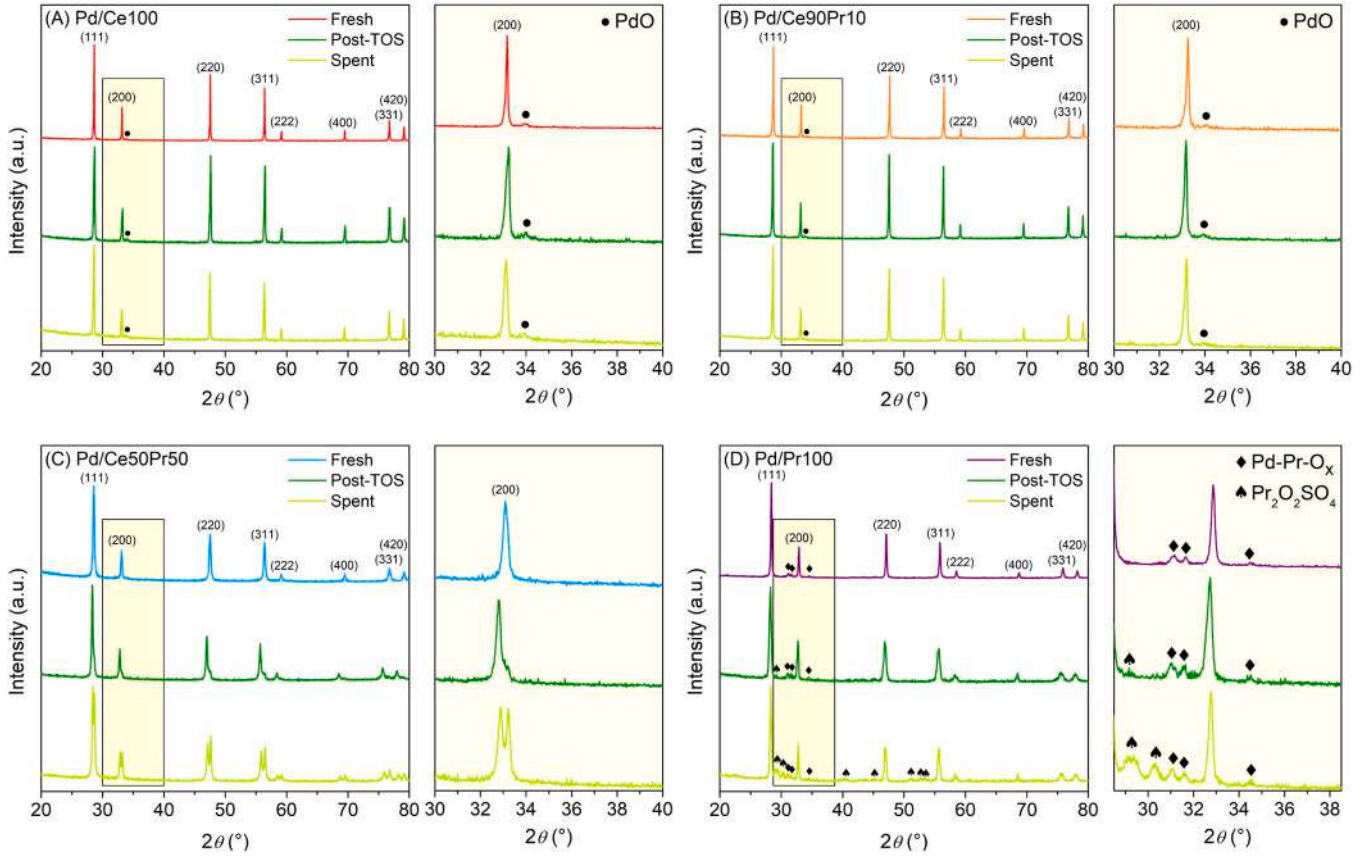


Fig. 9. Comparison of the X-ray diffractograms collected on the fresh, post-TOS, and spent Pd-based catalysts: Pd/Ce100 (A), Pd/Ce90Pr10 (B), Pd/Ce50Pr50 (C), and Pd/Pr100 (D). Magnifications of the 30° – 40° range are also reported to show the secondary phases (● ref. 00–041-1107, ◆ ref. 00–045-0528, ♠ ref. 00–041-067).

further Pr segregation induced by high-temperature treatment after sulfation. Notably, Pd remained relatively well dispersed. On the other hand, further Pd agglomeration was observed in spent Pd/Pr100 (Fig. 8B); however, Pd-rich clusters were poor in S (Area 3), while sulfur was preferentially distributed on the praseodymia support, forming sulfate aggregates mainly at the surface (Area 5), where the sulfur concentration was markedly higher than in the bulk (Area 4).

Possible structural modifications induced by sulfation were investigated by XRD and Raman spectroscopy. Fig. 9 compares the XRD patterns of fresh, post-TOS, and spent samples. No significant changes were detected for both Pd/Ce100 and Pd/Ce90Pr10, regarding either the fluorite pattern of ceria or the low-intensity PdO reflection at 34°. In contrast, sulfation strongly affected the structure of the Pr-rich catalysts. In Pd/Ce50Pr50, TOS sulfation induced a downward shift of the diffraction peaks toward lower angles, which can be attributed to the partial reduction of Ce^{4+} and Pr^{4+} to their larger trivalent ions during sulfation, as evidenced by XPS analysis, potentially combined with local lattice strain induced by sulfate formation. Notably, subsequent high-temperature treatment resulted in peak splitting, signaling the coexistence of two fluorite-like phases, which may result from the partial Pr segregation observed through STEM-EDX. Pd/Pr100 exhibited a similar peak shift after sulfation, due to Pr reduction, accompanied by an increased intensity of the Pd-Pr mixed oxide reflections [34,39]. Moreover, additional XRD peaks attributable to praseodymium sulfates appeared [66], which were particularly evident in the spent catalyst. These observations are consistent with XPS and EDX results, confirming that sulfur is not fully removed at high temperatures but instead reorganizes into larger, ordered sulfate domains.

Raman spectra of fresh and exhausted catalysts are compared in Fig. 10. Pd/Ce100 and Pd/Ce90Pr10 exhibited negligible spectral changes, confirming their high structural stability, in agreement with XRD results. Indeed, neither the ceria-related bands nor the PdO-related features showed significant variations (Fig. 10E), and the D/F_{2g} ratio remained essentially unchanged (Table 4). In contrast, Pd/Ce50Pr50 showed a pronounced increase in the defect-related band intensity after TOS, resulting in a substantial rise in the D/F_{2g} ratio (from approximately 2 to over 6). Although this ratio decreased slightly after high-temperature treatment (to ~ 4), the structure remained significantly more disordered than that of the fresh catalyst. The defect generation can be associated with Ce and Pr reduction, which accounts for the increase in oxygen vacancies concentration, as well as with sulfate formation, that can locally distort the fluorite lattice [32]. Structural changes in the Pd/Ce50Pr50 sample were also observed in HR-TEM images (Fig. S14). In Pd/Pr100, TOS induced moderate Raman spectral changes, including an increased intensity of the Pd-Pr mixed oxide band at 500 cm^{-1}, suggesting the progressive formation of this phase. Additionally, Raman features characteristic of praseodymium sulfate ($Pr_2(SO_4)_3$) were detected at ~995 and 1055 cm^{-1} in the spent sample (Fig. 10F) [67], confirming the formation of stable crystalline bulk sulfates.

DRIFTS spectra were collected on the fresh, post-TOS, and spent catalysts to further investigate the evolution of sulfur-containing species and other surface adsorbates (Fig. 11). All the fresh materials exhibit several contributions in the 1300 – 1600 cm^{-1} region, predominantly associated with carbonate species, with particularly prominent bands around 1380 and 1490 cm^{-1} in the Pr-rich samples [32]. The

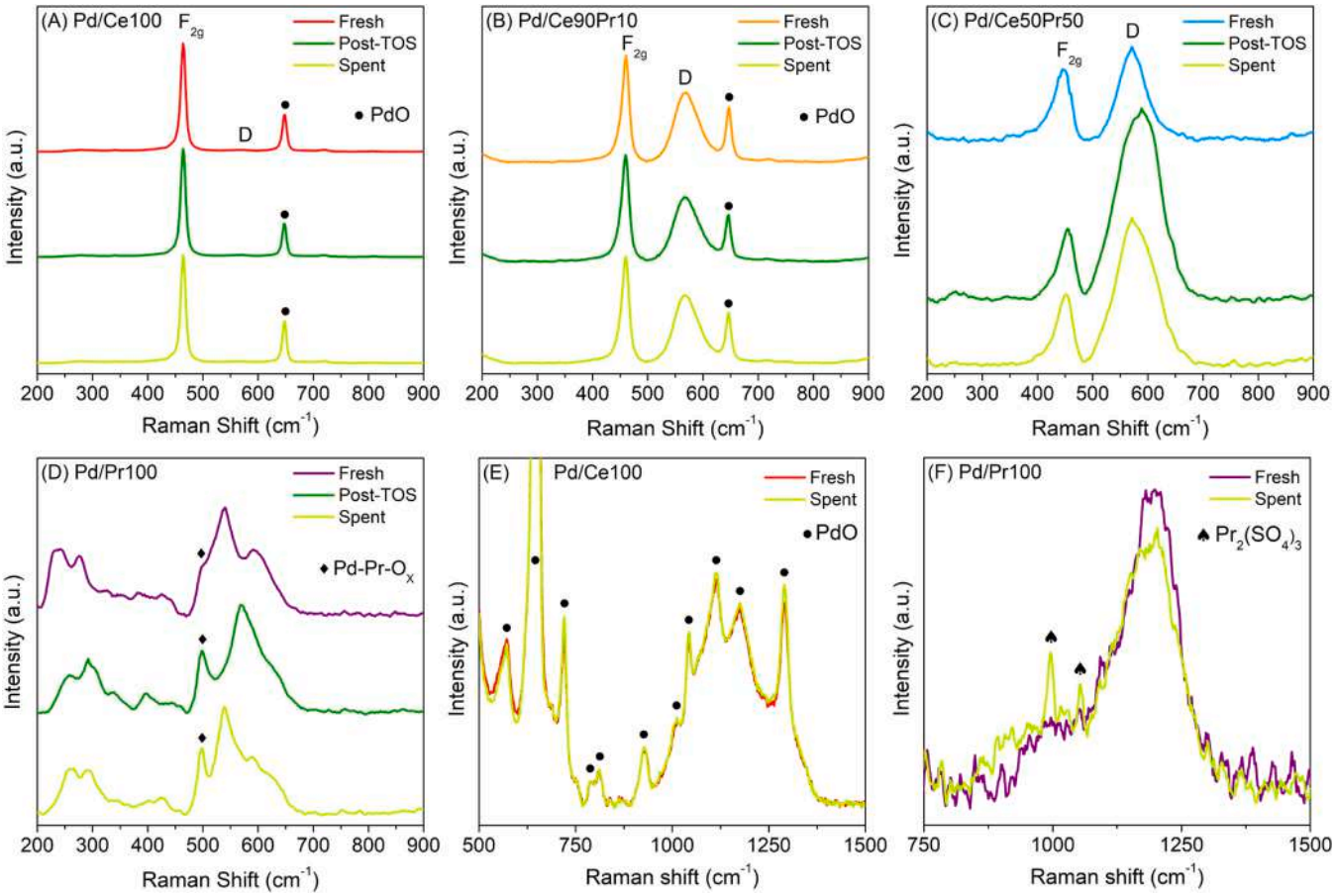


Fig. 10. Comparison of the Raman spectra collected on the fresh, post-TOS, and spent Pd-based catalysts: Pd/Ce100 (A), Pd/Ce90Pr10 (B), Pd/Ce50Pr50 (C), and Pd/Pr100 (D). Magnifications of the 500 – 1500 cm^{-1} range are also reported to show secondary peaks in Pd/Ce100 (E) and Pd/Pr100 (F). The corresponding D/F_{2g} values are reported in Table 4.

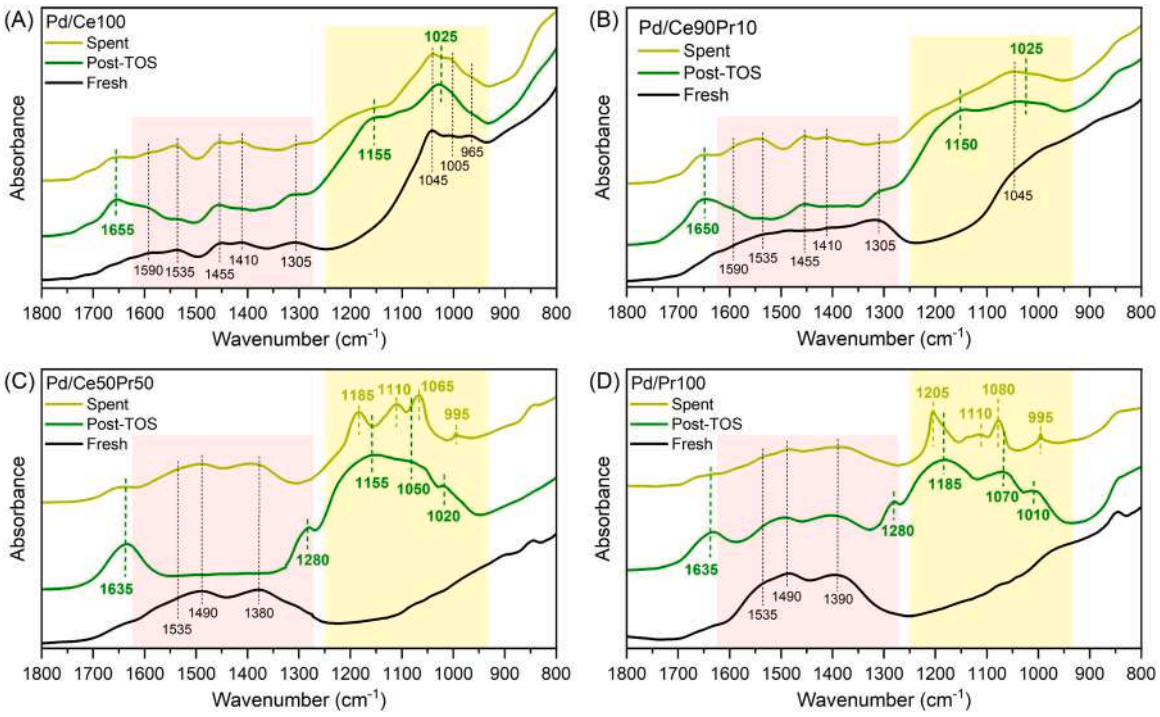


Fig. 11. Comparison of the DRIFTS spectra collected on the fresh, post-TOS, and spent Pd-based catalysts: Pd/Ce100 (A), Pd/Ce90Pr10 (B), Pd/Ce50Pr50 (C), and Pd/Pr100 (D). The pink region highlights the spectral range predominantly associated with carbonate-related bands, while the yellow region marks the range where the main S–O vibrations of sulfur-containing species are generally observed.

progressively higher intensity of these carbonate-related features upon Pr addition is consistent with the increased surface basicity of the Ce-Pr oxides [68]. Following SO_2 exposure, pronounced spectral changes occur mainly in the 950 – 1300 cm^{-1} region. Previous IR studies on ceria have assigned bands between approximately 1050 and 1250 cm^{-1} predominantly to S–O stretching vibrations of surface and bulk-like sulfate species, whereas contributions around 960 – 1000 cm^{-1} may also originate from sulfite species [53,65,69,70]. The development of these features in the post-TOS samples is therefore indicative of the formation of sulfur-containing compounds, that might be predominantly sulfate species considering the sulfur state identified by XPS. An additional feature around 1635 – 1655 cm^{-1} becomes considerably more intense after TOS, particularly for the Pr-containing catalysts. This band can be mainly assigned to the H–O–H bending vibration of adsorbed water [70], indicating that a significant amount of water was retained on the sulfated samples after TOS at 500 °C. This interpretation is also consistent with the DFT study of Auvinen et al., which predicted stronger H_2O adsorption on sulfated Pd surfaces [64].

Pd/Ce100 and Pd/Ce90Pr10 show a similar evolution upon SO_2 exposure. In both cases, sulfation results in the development of additional IR features around 1025 and 1150 – 1155 cm^{-1}, which lie within the region typically reported for S–O stretching of sulfate species, although contributions from sulfites cannot be completely excluded [53,65,69]. After high-temperature treatment, the spectra of both spent catalysts approach those of the corresponding fresh samples, in agreement with the substantial sulfur removal evidenced by elemental analysis and XPS and with the recovery of catalytic activity.

More pronounced changes in the DRIFTS spectra occur for Pd/Ce50Pr50 and Pd/Pr100. After TOS, a strong attenuation of the carbonate-related bands can be observed, accompanied by the development of intense absorption between approximately 950 and 1300 cm^{-1}. This behavior is consistent with the displacement of pre-adsorbed carbonates by sulfur-containing species during SO_2 exposure, as previously observed on ceria by Tumuluri et al. [53], in line with the strong interaction between S and Pr. In Pd/Ce50Pr50, the carbonate-related bands almost completely disappear after TOS and partly reappear in the spent catalyst, although with lower intensity than in the fresh material. At the same time, distinct bands at approximately 995, 1065, 1110, and 1185 cm^{-1} remain in the spent spectrum. Similarly, spent Pd/Pr100 exhibits only limited recovery of the carbonate-related region and retains pronounced features at approximately 995, 1080, 1110, and 1205 cm^{-1}. The persistence of S–O-related features in the Pr-rich catalysts confirms incomplete sulfur removal during high-temperature operation, while their evolution into more resolved components may be associated with the reorganization of the remaining sulfur species into larger sulfate domains, as suggested by XRD and Raman spectroscopy results.

The comprehensive characterization of the exhausted catalysts provides a coherent explanation of the role of Pr in influencing the sulfur-induced deactivation of Pd/ceria systems. As schematically illustrated in Fig. 12, exposure to traces of SO_2 during methane oxidation leads to direct sulfation of palladium supported on undoped ceria, causing rapid deactivation despite the low sulfur uptake. Owing to the stronger affinity of Pr for both Pd and S, mild Pr doping promotes the preferential reaction of SO_2 with the support; this effectively diverts sulfur away from the Pd active sites, protecting them from rapid poisoning and deactivation. The limited amount of formed sulfate species can be readily desorbed at high temperatures, allowing substantial recovery of catalytic activity and, in some cases, even enhancing activity through optimization of the Pd/PdO ratio. Instead, high Pr loadings not only induce excessively strong Pd-support interactions, that are detrimental to the PdO redox cycle and the Mars-van Krevelen-like mechanism, but also significantly increase the sulfur affinity of the catalyst. Although this protects Pd from direct poisoning, it results in extensive sulfate accumulation and Pr segregation from the ceria lattice, two phenomena that cannot be reversed by high-temperature treatment. These processes weaken the Pd-support interaction, promoting Pd reduction during thermal cycling, and, in the case of Pd/Pr100, even leading to partial Pd sintering. Overall, a mild Pr doping (10 at%) emerges as the optimal compromise to improve the activity and sulfur tolerance of Pd/ceria

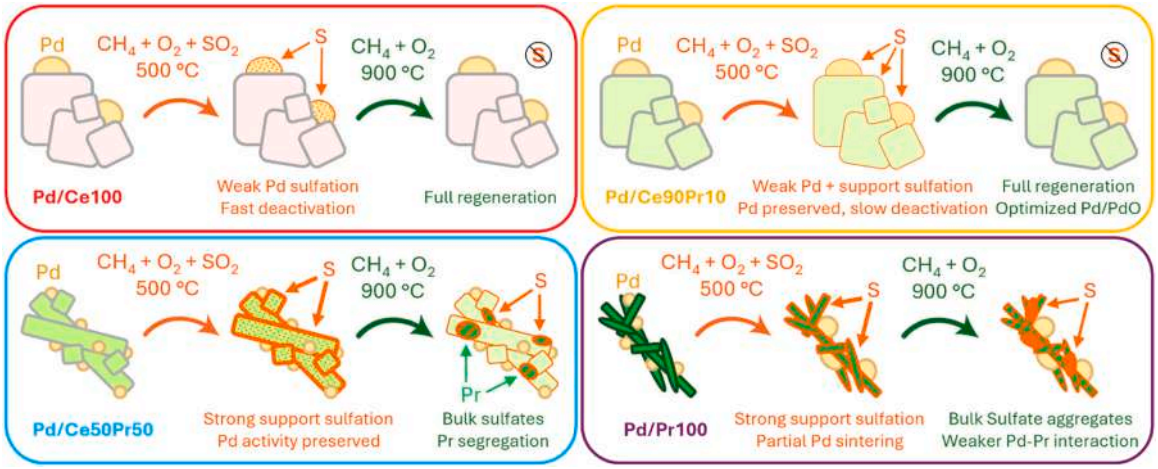


Fig. 12. Schematic of sulfation mechanisms over the four Pd-based catalysts presented in this work.

catalysts, while preserving structural stability and regenerability under high-temperature operation.

3.4. Effect of water

Since water is a major component of combustion exhaust gases, catalytic activity and SO_2 poisoning tests were also performed under wet conditions, following the same protocol adopted for the dry experiments (Fig. 1) but adding 5% H_2O to the reaction mixture throughout the entire test. The results obtained for Pd/Ce100 and Pd/Ce90Pr10 are reported in Fig. 13. In the presence of water, the activity of both fresh catalysts (i.e., in the 2nd heating/cooling cycle) decreased, with the light-off curves shifting toward higher temperatures and a more pronounced activity loss above 700 °C associated with PdO decomposition (Fig. 13A and B).

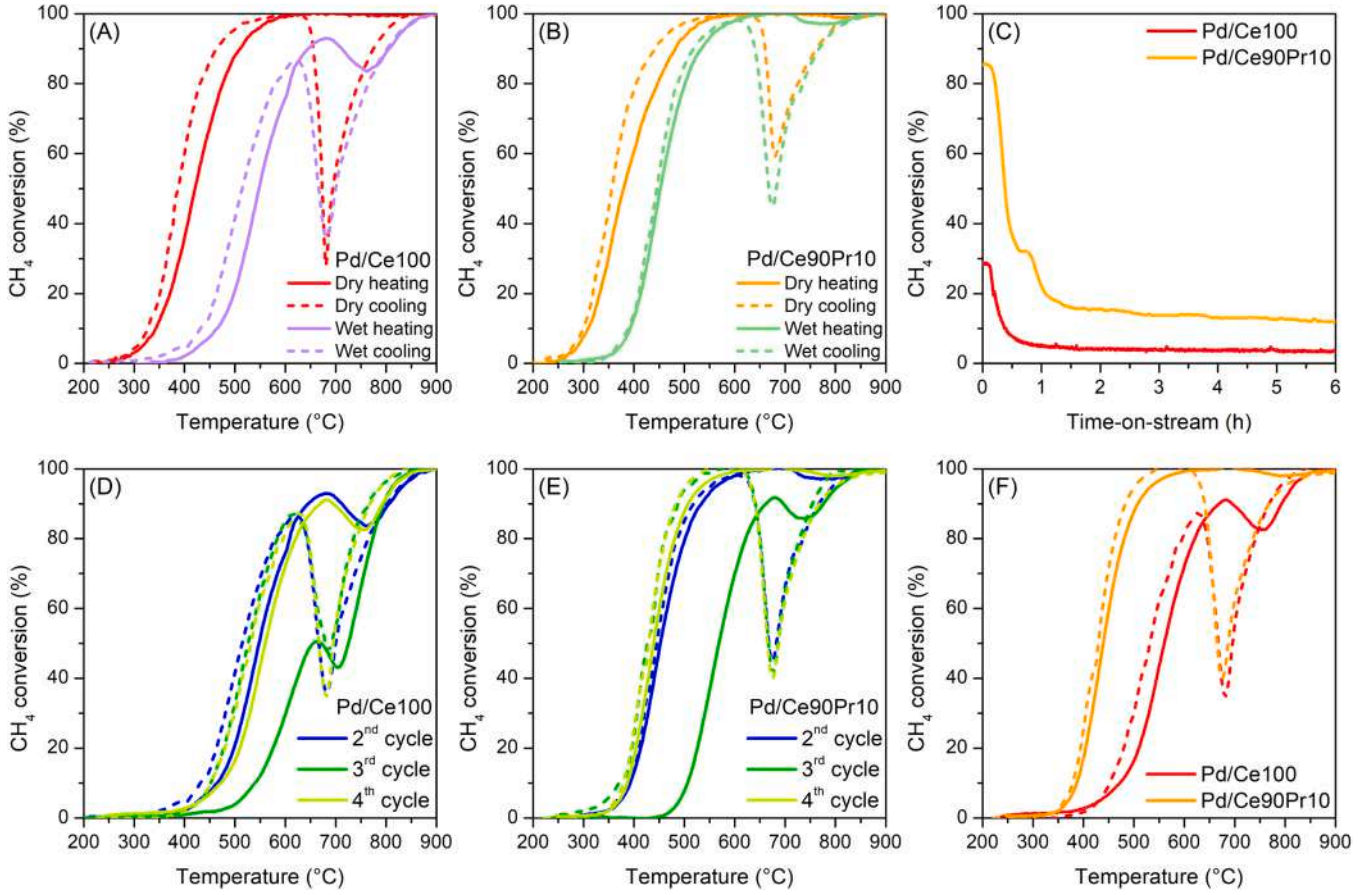


Fig. 13. Comparison of methane conversion curves obtained in dry and wet conditions (wet feed: 0.3% CH_4 + 1.2% O_2 + 5.0% H_2O in N_2) during the 2nd cycle over Pd/Ce100 (A) and Pd/Ce90Pr10 (B). Evolution of CH_4 conversion over time during the TOS stage (C), performed in wet conditions at 500 °C in the presence of 20 ppm of SO_2. Methane conversion curves as a function of temperature during heating (solid lines) and cooling (dashed lines) of the 2nd, 3rd, and 4th cycles of wet methane oxidation over Pd/Ce100 (D) and Pd/Ce90Pr10 (E). Comparison of the conversion curves of the two catalysts during the 4th heating (solid lines) and cooling (dashed lines) cycle in wet conditions (F).

Water inhibition is well established for Pd-based methane oxidation catalysts and is generally attributed to competitive adsorption and to the formation of surface hydroxyl species, which block sites involved in methane activation and interfere with PdO redox dynamics [24,25]. However, this effect was less pronounced for Pd/Ce90Pr10, in agreement with previous investigations of this catalytic system: indeed, moderate Pr incorporation was shown to optimize the hydrophobic/hydrophilic balance of the catalyst surface, thus mitigating water inhibition [34]. Consequently, the beneficial effect of mild Pr doping becomes particularly relevant under wet reaction conditions.

Fig. 13C shows the evolution of methane conversion over time during the TOS stage at 500 °C performed in wet conditions. Upon addition of 20 ppm of SO_2, the conversion over Pd/Ce100 rapidly decreased from 29% to 8% within 30 min and then progressively declined to 3.5% after 6 h. Pd/Ce90Pr10 remained considerably more active in absolute terms, but its deactivation was markedly faster than under dry conditions, with CH_4 conversion decreasing from 86% to 22% after 1 h and to 12% after 6 h. Therefore, although Pd/Ce90Pr10 still exhibited higher residual activity than Pd/Ce100, the significant advantage in sulfur tolerance observed under dry conditions was substantially attenuated by the presence of water. Indeed, after 6 h the two catalysts retained similar fractions of their initial activity (ca. 12–14%), as indicated by the corresponding methane reaction rates reported in Table S2.

Such behavior is consistent with previous studies reporting a coupled detrimental effect of H_2O and SO_2 on Pd-based methane oxidation catalysts. Water has indeed been shown to accelerate sulfur-induced deactivation and sulfate formation, by modifying sulfur adsorption and redistribution between Pd and the support. In particular, Mowery and McCormick observed that water can interfere with the sulfur-scavenging ability of the support in Pd/Al_2O_3 catalysts, by displacing SO_2 from alumina sites and inhibiting sulfur spillover from PdO to the support, thereby accelerating $PdSO_4$ formation [63]. A similar mechanism could occur in the present system, where competitive adsorption and hydroxylation of the Ce-Pr oxide surface may partially hinder its ability to divert sulfur species from PdO toward the support, thereby weakening the protective role of Pr observed under dry conditions. At the same time, sulfated Pd sites may become more sensitive to water inhibition. Indeed, Pd sulfation can decrease oxygen mobility and hinder water desorption [71], while strongly adsorbed H_2O and hydroxyl species on the layer of Pd sulfate at the catalyst surface can further inhibit methane activation [64]. The interplay among all these effects may therefore be responsible for the altered deactivation behavior of Pd/Ce90Pr10 under wet conditions.

The light-off curves obtained before SO_2 exposure (2^{nd} cycle) and after the TOS stage (3^{rd} and 4^{th} cycles) are compared in Figs. 13D and 13E. The overall behavior was similar to that observed under dry conditions. Both catalysts exhibited lower activity during the 3^{rd} heating run with respect to the 2^{nd} one, with the light-off curves shifted by approximately 100 °C toward higher temperatures due to sulfur poisoning. However, catalytic activity was substantially recovered after reaching high temperature. For Pd/Ce100, the 4^{th} cycle profile closely approached that of the fresh sample (Fig. 13D), whereas Pd/Ce90Pr10 exhibited slightly higher activity during the 4^{th} heating run than in the fresh state (Fig. 13E). After high-temperature treatment, Pd/Ce90Pr10 also remained markedly more active than Pd/Ce100, with the difference between the two catalysts being even more evident under wet conditions (Fig. 13F).

Overall, these results are consistent with those obtained under dry conditions and indicate that the sulfur-induced activity loss of the Ce-rich catalysts can be substantially reversed through high-temperature treatment. Nevertheless, under wet conditions, the beneficial effect of mild Pr doping on sulfur tolerance is considerably reduced, highlighting an important interplay between water inhibition and sulfur poisoning.

4. Conclusions

In this work, the role of Pr doping in affecting the sulfur tolerance of Pd/ceria-based catalysts for complete methane oxidation was systematically investigated. Four Pd-containing samples with different Pr contents were compared through multi-step catalytic tests, consisting of four heating-cooling cycles interposed by a time-on-stream stage in the presence of SO_2. An extensive multi-technique characterization was performed on the fresh and exhausted materials, including samples obtained after the TOS exposure to SO_2 and after further cycles of methane oxidation.

Undoped Pd/CeO_2 was highly sensitive to S poisoning, despite its low sulfur uptake. STEM-EDX mapping pointed out that SO_2 preferentially interacted with the Pd particles, leading to the formation of sulfates directly on the Pd active sites and causing fast deactivation. However, these species were efficiently removed during subsequent high-temperature treatment, allowing for the partial recovery of the initial activity.

The introduction of praseodymium into the ceria lattice markedly altered the sulfur-catalyst interactions. A mild Pr doping (10 at%) effectively diverted sulfur from Pd toward the support, due to the higher Pr-S affinity. In this case, sulfates were homogeneously distributed over the oxide matrix rather than selectively accumulated on Pd, resulting in slower deactivation. Importantly, the limited amount of sulfates formed was readily desorbed during high-temperature reaction, while a slightly weakened Pd-support interaction resulted in improved activity due to an optimized Pd/PdO ratio. As a result, the Pd/Ce90Pr10 sample offered the best compromise between catalytic performance, sulfur tolerance, and structural stability.

At higher Pr loadings, the increased sulfur affinity of the support effectively protected Pd from direct poisoning, but at the expense of extensive sulfate accumulation. The strong sulfation promoted catalyst reduction and induced partial segregation of Pr from the ceria lattice. These structural changes weakened the Pd-support interaction, favoring Pd reduction during high-temperature methane oxidation and, in the case of the pure praseodymia support, even leading to Pd sintering. Moreover, the sulfates were not completely removed during thermal treatment, but instead reorganized into stable bulk aggregates, contributing to increased lattice disorder. As a consequence, excessive Pr doping resulted in irreversible structural modifications that ultimately compromised catalytic activity at high temperatures.

Overall, this study demonstrates that praseodymium acts as a sulfur scavenger in Pd/ceria catalysts, but that its beneficial effect is strongly dependent on its concentration. While moderate Pr doping significantly enhances sulfur resistance and preserves the catalyst ability to be regenerated, excessive Pr loadings lead to detrimental structural and chemical changes within the catalyst upon sulfation. These findings reveal how the praseodymium content can be strategically tuned to balance metal-support interactions, sulfur affinity, and redox functionality, providing valuable guidelines for the rational design of sulfur-tolerant catalysts for methane oxidation.

CRediT authorship contribution statement

Enrico Sartoretti: Conceptualization, Data curation, Formal analysis, Funding acquisition, Investigation, Methodology, Writing – original draft, Writing – review & editing, Supervision. **Eleonora Calì:** Investigation, Methodology, Writing – review & editing, Data curation, Formal analysis. **Chiara Novara:** Methodology, Writing – review & editing, Formal analysis. **Fabrizio Giorgis:** Resources, Writing – review & editing. **Marco Piumetti:** Formal analysis, Supervision, Writing – review & editing. **Debora Fino:** Resources, Writing – review & editing. **Nunzio Russo:** Formal analysis, Resources, Supervision, Writing – review & editing. **Samir Bensaid:** Conceptualization, Formal analysis, Funding acquisition, Methodology, Resources, Supervision, Writing – review & editing.

Declaration of Competing Interest

The authors declare that they have no known competing financial interests or personal relationships that could have appeared to influence the work reported in this paper.

Acknowledgements

The authors kindly thank Enrico Lanzilotti and Gabriele Monteu Richiardi for helping in data collection during the preparation of their MS theses, and Camilla Galletti for performing XRD. The authors acknowledge CERIC-ERIC for providing access to the HoloTEM facility at the University of Salento under proposal 20242024. The authors also gratefully thank Prof. Daniela Manno for conducting the HoloTEM measurements and providing valuable technical support. The Italian Ministero dell'Università e della Ricerca (MUR) is also acknowledged for the funding received under the Dipartimento di Eccellenza 2018–2022 program and the PON Ricerca e Innovazione "REACT-EU" project (DM 1062/21).

Appendix A. Supporting information

Supplementary data associated with this article can be found in the online version at doi:10.1016/j.apcatb.2026.127701.

Data Availability

Data will be made available on request.

References

[1] S.J.M. Algayyim, K. Saleh, A.P. Wandel, I.M.R. Fattah, T. Yusaf, H.A. Alrazen, Influence of natural gas and hydrogen properties on internal combustion engine performance, combustion, and emissions: a review, Fuel 362 (2024) 130844, https://doi.org/10.1016/J.FUEL.2023.130844.

[2] T.C. Zannis, J.S. Katsanis, G.P. Christopoulos, E.A. Yfantis, R.G. Papagiannakis, E. G. Pariotis, D.C. Rakopoulos, C.D. Rakopoulos, A.G. Vallis, Marine exhaust gas treatment systems for compliance with the IMO 2020 Global Sulfur Cap and Tier III NOx Limits: a review, Energies 15 (2022) 3638, https://doi.org/10.3390/en15103638.

[3] A. Christodoulou, K. Cullinane, Potential alternative fuel pathways for compliance with the 'FuelEU Maritime Initiative, Transp. Res. Part. D. Transp. Environ. 112 (2022) 103492, https://doi.org/10.1016/J.TRD.2022.103492.

[4] P. Vedele, E. Sartoretti, G. Torretti, C. Novara, F. Salomone, F. Giorgis, M. Antonini, S. Bensaid, Thermocatalytic methane pyrolysis over iron-based catalysts for turquoise hydrogen production: activity and kinetic studies, Chem. Eng. J. (2025) 163392, https://doi.org/10.1016/j.cej.2025.163392.

[5] S. Bakkaloglu, A. Hawkes, A comparative study of biogas and biomethane with natural gas and hydrogen alternatives, Energy Environ. Sci. 17 (2024) 1482–1496, https://doi.org/10.1039/D3EE02516K.

[6] F. Celoria, F. Salomone, A. Tauro, M. Gandiglio, D. Ferrero, I. Champon, G. Geffraye, R. Pirone, S. Bensaid, Kinetic study and deactivation phenomena for the methanation of CO_2 and CO mixed syngas on a Ni/Al_2O_3 catalyst, Chem. Eng. J. 512 (2025) 162113, https://doi.org/10.1016/J.CEJ.2025.162113.

[7] T. Skytt, S.N. Nielsen, B.G. Jonsson, Global warming potential and absolute global temperature change potential from carbon dioxide and methane fluxes as indicators of regional sustainability – a case study of Jämtland, Sweden, Ecol. Indic. 110 (2020) 105831, https://doi.org/10.1016/J.ECOLIND.2019.105831.

[8] A. Huonder, D. Olsen, Methane emission reduction technologies for natural gas engines: a review, 2023, Vol. 16, Page 7054, Energies 16 (2023) 7054, https://doi.org/10.3390/EN16207054.

[9] P. Gélin, M. Primet, Complete oxidation of methane at low temperature over noble metal based catalysts: a review, Appl. Catal. B Environ. 39 (2002) 1–37, https://doi.org/10.1016/S0926-3373(02)00076-0.

[10] D. Ciuparu, M.R. Lyubovsky, E. Altman, L.D. Pfefferle, A. Datye, Catalytic combustion of methane over palladium-based catalysts, Catal. Rev. - Sci. Eng. 44 (2002) 593–649, https://doi.org/10.1081/CR-120015482.

[11] A. Hellman, A. Resta, N.M. Martin, J. Gustafson, A. Trinchero, P.A. Carlsson, O. Balmes, R. Felici, R. Van Rijn, J.W.M. Frenken, J.N. Andersen, E. Lundgren, H. Grönbeck, The active phase of palladium during methane oxidation, J. Phys. Chem. Lett. 3 (2012) 678–682, https://doi.org/10.1021/jz300069s.

[12] E.D. Goodman, A.A. Ye, A. Aitbekova, O. Mueller, A.R. Riscoe, T. Nguyen Taylor, A.S. Hoffman, A. Boubnov, K.C. Bustillo, M. Nachtegaal, S.R. Bare, M. Cargnello, Palladium oxidation leads to methane combustion activity: effects of particle size and alloying with platinum, J. Chem. Phys. 151 (2019) 154703, https://doi.org/10.1063/1.5126219.

[13] M. Danielis, N.J. Divins, J. Llorca, L. Soler, X. Garcia, I. Serrano, L.E. Betancourt, W. Xu, J.A. Rodríguez, S.D. Senanayake, S. Colussi, A. Trovarelli, situ investigation of the mechanochemically promoted Pd–Ce interaction under stoichiometric methane oxidation conditions, EES Catal. 1 (2023) 144–152, https://doi.org/10.1039/d2ey00067a.

[14] S. Yue, C.S. Praveen, A. Klyushin, A. Fedorov, M. Hashimoto, Q. Li, T. Jones, P. Liu, W. Yu, M.G. Willinger, X. Huang, Redox dynamics and surface structures of an active palladium catalyst during methane oxidation, Nat. Commun. 15 (2024) 4678, https://doi.org/10.1038/s41467-024-49134-y.

[15] S.H. Ryu, S. Choung, Y. Choi, H. Lee, J.H. Choi, J.W. Han, H. Jeong, Partially reduced PdO_x nanoparticles strongly interacting with defect-rich ceria via dynamic redox pulse for complete methane oxidation, Appl. Catal. B Environ. 379 (2025) 125672, https://doi.org/10.1016/j.apcatb.2025.125672.

[16] M. Danielis, S. Colussi, C. De Leitenburg, A. Trovarelli, The role of palladium salt precursors in Pd-PdO/CeO_2 catalysts prepared by dry milling for methane oxidation, Catal. Commun. 135 (2020) 105899, https://doi.org/10.1016/j.catcom.2019.105899.

[17] S. Colussi, P. Fornasiero, A. Trovarelli, Structure-activity relationship in Pd/CeO_2 methane oxidation catalysts, Chin. J. Catal. 41 (2020) 938–950, https://doi.org/10.1016/S1872-2067(19)63510-2.

[18] V. Muravev, A. Parastaev, Y. van den Bosch, B. Ligt, N. Claes, S. Bals, N. Kosinov, E. J.M. Hensen, Size of cerium dioxide support nanocrystals dictates reactivity of highly dispersed palladium catalysts, Science (80-) 380 (2023) 1174–1178, https://doi.org/10.1126/science.adf9082.

[19] Y. Ding, Y. Jia, M. Jiang, Y. Guo, Y. Guo, L. Wang, Q. Ke, M. Ngoc, S. Dai, W. Zhan, Superior catalytic activity of Pd-based catalysts upon tuning the structure of the ceria-zirconia support for methane combustion, Chem. Eng. J. 416 (2021) 129150, https://doi.org/10.1016/j.cej.2021.129150.

[20] D. Zengel, V. Marchuk, M. Kurt, F. Maurer, A. Salcedo, C. Michel, D. Loffreda, M. Aouine, S. Loridant, P. Vernoux, H. Stormer, M. Casapu, J.-D. Grunwaldt, Pd loading threshold for an efficient noble metal use in Pd/CeO_2 methane oxidation catalysts, Appl. Catal. B Environ. Energy 358 (2024), https://doi.org/10.1016/j.apcatb.2024.124363.

[21] M. Danielis, S. Colussi, C. De Leitenburg, L. Soler, J. Llorca, A. Trovarelli, Outstanding methane oxidation performance of palladium-embedded ceria catalysts prepared by a one-step dry ball-milling method, Angew. Chem. - Int. Ed. 57 (2018) 10212–10216, https://doi.org/10.1002/anie.201805929.

[22] Y. Chen, Y. Luo, X. Yang, Q. Zhao, Y. Fan, Y. Liu, J. Yi, Research progress on the deactivation mechanism and suppression strategies of Pd-based catalysts for methane oxidation, Catal. Sci. Technol. 15 (2025) 5226–5255, https://doi.org/10.1039/d5cy00498e.

[23] M. Giuliano, M.C. Valsania, P. Ticali, E. Sartoretti, S. Morandi, S. Bensaid, G. Ricchiardi, M. Sgroi, Characterization of the evolution of noble metal particles in a commercial three-way catalyst: correlation between real and simulated ageing, Catalysts 11 (2021) 1–15, https://doi.org/10.3390/catal11020247.

[24] R. Gholami, M. Alyani, K.J. Smith, Deactivation of Pd catalysts by water during low temperature methane oxidation relevant to natural gas vehicle converters, Catalysts 5 (2015) 561–594, https://doi.org/10.3390/catal5020561.

[25] W. Huang, E.D. Goodman, P. Losch, M. Cargnello, Deconvoluting transient water effects on the activity of Pd methane combustion catalysts, Ind. Eng. Chem. Res. 57 (2018) 10261–10268, https://doi.org/10.1021/acs.iecr.8b01915.

[26] R.L. Arevalo, S.M. Aspera, H. Nakanishi, Sulfation of a PdO(101) methane oxidation catalyst: mechanism revealed by first principles calculations, Catal. Sci. Technol. 9 (2019) 232–240, https://doi.org/10.1039/C8CY02096E.

[27] T. Delrieux, S. Sharma, F. Maurer, J. Czechowsky, C.N. Borca, D. Karpov, C. Camilo, P. Lott, M. Casapu, T.L. Sheppard, J. Grunwaldt, Tracking sulfur poisoning of Pd/Al2O3 catalysts for methane oxidation on different complexity scales, ACS Catal. 15 (2025) 13470–13485, https://doi.org/10.1021/acscatal.5c02678.

[28] W. Yang, M. Kim, F. Polo-garzon, J. Gong, X. Jiang, Z. Huang, M. Chi, X. Yu, X. Wang, Y. Guo, Z. Wu, CH_4 combustion over a commercial Pd/CeO_2-ZrO2 three-way catalyst: impact of thermal aging and sulfur exposure, Chem. Eng. J. 451 (2023) 138930, https://doi.org/10.1016/j.cej.2022.138930.

[29] P. Lott, M. Eck, D.E. Doronkin, A. Zimina, S. Tischer, R. Popescu, S. Belin, V. Briois, M. Casapu, J.D. Grunwaldt, O. Deutschmann, Understanding sulfur poisoning of bimetallic Pd-Pt methane oxidation catalysts and their regeneration, Appl. Catal. B Environ. 278 (2020) 119244, https://doi.org/10.1016/J.APCATB.2020.119244.

[30] J. Lin, X. Chen, Y. Zheng, Y. Xiao, Y. Zheng, L. Jiang, Sulfur-resistant methane combustion invoked by surface property regulation on palladium-based catalysts, Appl. Surf. Sci. 587 (2022) 152835, https://doi.org/10.1016/j.apsusc.2022.152835.

[31] W. Yang, Y. Wu, X. Zheng, H. Xu, J. Wang, Y. Chen, Enhanced water and sulfur resistance of a palladium / ceria-zirconia catalyst for low-concentration methane combustion through silicate modifying support properties, Sep. Purif. Technol. 373 (2025) 133447, https://doi.org/10.1016/j.seppur.2025.133447.

[32] Y. Ding, S. Wang, L. Zhang, L. Lv, D. Xu, W. Liu, S. Wang, Investigation of supported palladium catalysts for combustion of methane: the activation effect caused by SO_2, Chem. Eng. J. 382 (2020) 122969, https://doi.org/10.1016/j.cej.2019.122969.

[33] S. Ballauri, E. Sartoretti, C. Novara, F. Giorgis, M. Piumetti, D. Fino, N. Russo, S. Bensaid, Wide range temperature stability of palladium on ceria-praseodymia catalysts for complete methane oxidation, Catal. Today 390–391 (2022) 185–197, https://doi.org/10.1016/j.cattod.2021.11.035.

[34] S. Ballauri, E. Sartoretti, M. Hu, C. D'Agostino, Z. Ge, L. Wu, C. Novara, F. Giorgis, M. Piumetti, D. Fino, N. Russo, S. Bensaid, Praseodymium doping in ceria-supported palladium nanocatalysts as an effective strategy to minimize the

inhibiting effects of water during methane oxidation, Appl. Catal. B Environ. 320 (2023) 121898, https://doi.org/10.1016/j.apcatb.2022.121898.
[35] S. Ballauri, E. Sartoretti, M. Castellino, M. Armandi, M. Piumetti, D. Fino, N. Russo, S. Bensaid, Mesoporous ceria and ceria-praseodymia as high surface area supports for Pd-based catalysts with enhanced methane oxidation activity, ChemCatChem 16 (2024) e202301359, https://doi.org/10.1002/cctc.202301359.
[36] E. Sartoretti, F.P. Hagen, C. Novara, M. Piumetti, H. Bockhorn, D. Trimis, S. Bensaid, Rare-earth-doped ceria nanostructures for oxidation of soot with different reactivities: role of catalyst restructuring and surface acidity in soot-catalyst contact renewal, J. Environ. Chem. Eng. 14 (2026) 123057, https://doi.org/10.1016/j.jece.2026.123057.
[37] A. Rizzetto, M.Pietro Mezzapesa, F. Celoria, F. Salomone, E. Sartoretti, M. Piumetti, R. Pirone, S. Bensaid, Low-content Ru catalysts for efficient CO_2 methanation, ChemCatChem (2025) e01275, https://doi.org/10.1002/CCTC.202501275.
[38] A. Baylet, P. Marécot, D. Duprez, P. Castellazzi, G. Groppi, P. Forzatti, situ Raman and in situ XRD analysis of PdO reduction and Pd° oxidation supported on γ-Al_2O_3 catalyst under different atmospheres, Phys. Chem. Chem. Phys. 13 (2011) 4607–4613, https://doi.org/10.1039/c0cp01331e.
[39] T.C. Chou, T. Kennelly, R.J. Farrauto, US Patent 5 169 300: Praseodymium-palladium binary oxide, catalyst, methods of combustion and regeneration, 1992.
[40] J.R. McBride, K.C. Hass, W.H. Weber, Resonance-Raman and lattice-dynamics studies of single-crystal PdO, Phys. Rev. B. 44 (1991) 5016–5028.
[41] A. García-Cuenca, I. Mekki, A. García-García, Effect of copper and manganese as active phases in ceria and ceria-praseodymia catalysts for soot combustion in the exhaust of Gasoline Direct Injection (GDI) vehicles, Appl. Catal. B Environ. 370 (2025) 125180, https://doi.org/10.1016/j.apcatb.2025.125180.
[42] E. Sartoretti, C. Novara, M. Fontana, F. Giorgis, M. Piumetti, S. Bensaid, N. Russo, D. Fino, New insights on the defect sites evolution during CO oxidation over doped ceria nanocatalysts probed by in situ Raman spectroscopy, Appl. Catal. A Gen. 596 (2020) 117517, https://doi.org/10.1016/j.apcata.2020.117517.
[43] N. Guillén-Hurtado, J. Giménez-Mañogil, J.C. Martínez-Munuera, A. Bueno-López, A. García-García, Study of Ce/Pr ratio in ceria-praseodymia catalysts for soot combustion under different atmospheres, Appl. Catal. A Gen. 590 (2020) 117339, https://doi.org/10.1016/j.apcata.2019.117339.
[44] G. Pampararo, E. Sartoretti, A.S. Traoré, O. Ersen, C. Novara, S. Bensaid, D. P. Debecker, Spray-made porous CuO-CeO_2 microspheres rival precious metal catalysts for the low-temperature oxidation of air pollutants, J. Environ. Chem. Eng. 13 (2025) 116753, https://doi.org/10.1016/j.jece.2025.116753.
[45] R.D. Shannon, Revised effective ionic radii and systematic studies of interatomic distances in halides and chalcogenides, Acta Crystallogr. Sect. A. 32 (1976) 751–767, https://doi.org/10.1107/S0567739476001551.
[46] X. Garcia, L. Soler, X. Vendrell, I. Serrano, F. Herrera, J. Prat, E. Solano, M. Tallarida, J. Llorca, C. Escudero, Operando NAP-XPS studies of a ceria-supported Pd catalyst for CO oxidation, Chem 5 (2023) 1–18, https://doi.org/10.3390/chemistry5010001.
[47] A. Westermann, C. Geantet, P. Vernoux, S. Loridant, Defects band enhanced by resonance Raman effect in praseodymium doped CeO_2, J. Raman Spectrosc. 47 (2016) 1276–1279, https://doi.org/10.1002/jrs.4943.
[48] L. Chen, P. Fleming, V. Morris, J.D. Holmes, M.A. Morris, Size-related lattice parameter changes and surface defects in ceria nanocrystals, J. Phys. Chem. C. 114 (2010) 12909–12919, https://doi.org/10.1021/jp1031465.
[49] S. Colussi, A. Trovarelli, E. Vesselli, A. Baraldi, G. Comelli, G. Groppi, J. Llorca, Structure and morphology of Pd/Al_2O_3 and Pd/CeO_2/Al_2O_3 combustion catalysts in Pd-PdO transformation hysteresis, Appl. Catal. A Gen. 390 (2010) 1–10, https://doi.org/10.1016/j.apcata.2010.09.033.
[50] H. Xiong, D. Kunwar, D. Jiang, C.E. García-Vargas, H. Li, C. Du, G. Canning, X. I. Pereira-Hernandez, Q. Wan, S. Lin, S.C. Purdy, J.T. Miller, K. Leung, S.S. Chou, H.H. Brongersma, R. ter Veen, J. Huang, H. Guo, Y. Wang, A.K. Datye, Engineering catalyst supports to stabilize PdO_x two-dimensional rafts for water-tolerant methane oxidation, Nat. Catal. 4 (2021) 830–839, https://doi.org/10.1038/s41929-021-00680-4.
[51] F. Kong, B. Nie, X. Luo, L. Jiang, Z. Shao, J. Huang, Mitigating methane emissions: Analyzing the microstructural evolution of Pd-based membranes under lean methane oxidation conditions, Fuel 389 (2025) 134618, https://doi.org/10.1016/J.FUEL.2025.134618.
[52] J. Nilsson, P.A. Carlsson, S. Fouladvand, N.M. Martin, J. Gustafson, M.A. Newton, E. Lundgren, H. Grönbeck, M. Skoglundh, Chemistry of supported palladium nanoparticles during methane oxidation, ACS Catal. 5 (2015) 2481–2489, https://doi.org/10.1021/cs502036d.
[53] U. Tumuluri, M. Li, B.G. Cook, B. Sumpter, S. Dai, Z. Wu, Surface structure dependence of SO2 interaction with ceria nanocrystals with well-defined surface facets, J. Phys. Chem. C. 119 (2015) 28895–28905, https://doi.org/10.1021/acs.jpcc.5b07946.
[54] Y. Lei, W. Li, Q. Liu, Q. Lin, X. Zheng, Q. Huang, S. Guan, X. Wang, C. Wang, F. Li, Typical crystal face effects of different morphology ceria on the activity of Pd/CeO_2 catalysts for lean methane combustion, Fuel 233 (2018) 10–20, https://doi.org/10.1016/J.FUEL.2018.06.035.
[55] M.Y. Smirnov, A.V. Kalinkin, A.V. Pashis, A.M. Sorokin, A.S. Noskov, V. I. Bukhtiyarov, K.C. Kharas, M.A. Rodkin, Comparative XPS study of Al2O3 and CeO2 sulfation in reactions with SO2, SO2 + O2, SO2 + H2O, and SO2 + O2 + H2O, Ki, Net. Catal. 44 (2003) 575–582.
[56] J.D. Henderson, B.P. Payne, N.S. McIntyre, M.C. Biesinger, Enhancing oxygen spectra interpretation by calculating oxygen linked to adventitious carbon, Surf. Interface Anal. 57 (2025) 214–220, https://doi.org/10.1002/sia.7376.
[57] N. Grifasi, E. Sartoretti, P. Legutko, S. Bensaid, N. Russo, A. Adamski, D. Fino, M. Piumetti, Copper-manganese oxide catalysts for low-temperature oxidation of indoor pollutants, Appl. Catal. B Environ. 385 (2026) 126292, https://doi.org/10.1016/j.apcatb.2025.126292.
[58] F. Salomone, G. Bonura, F. Frusteri, M. Castellino, M. Fontana, A.M. Chiodoni, N. Russo, R. Pirone, S. Bensaid, Physico-chemical modifications affecting the activity and stability of Cu-based hybrid catalysts during the direct hydrogenation of carbon dioxide into dimethyl-ether, Materials (Basel) 15 (2022) 7774, https://doi.org/10.3390/ma15217774.
[59] N. Grifasi, E. Sartoretti, D. Montesi, S. Bensaid, N. Russo, F. Deorsola, D. Fino, C. Novara, F. Giorgis, M. Piumetti, Mesostructured manganese oxides for efficient catalytic oxidation of CO, ethylene, and propylene at mild temperatures: insight into the role of crystalline phases and physico-chemical properties, Appl. Catal. B Environ. Energy 362 (2025) 124696, https://doi.org/10.1016/j.apcatb.2024.124696.
[60] D.J. Morgan, Photoelectron spectroscopy of ceria: reduction, quantification and the myth of the vacancy peak in XPS analysis, Surf. Interface Anal. 55 (2023) 845–850, https://doi.org/10.1002/sia.7254.
[61] A. Rizzetto, M. Piumetti, R. Pirone, E. Sartoretti, S. Bensaid, Study of ceria-composite materials for high-temperature CO_2 capture and their ruthenium functionalization for methane production, Catal. Today 429 (2024) 114478, https://doi.org/10.1016/j.cattod.2023.114478.
[62] E. Poggio-Fraccari, G. Baronetti, F. Mariño, Pr^{3+} surface fraction in CePr mixed oxides determined by XPS analysis, J. Electron. Spectros. Relat. Phenom. 222 (2018) 1–4, https://doi.org/10.1016/j.elspec.2017.11.003.
[63] D.L. Mowery, R.L. McCormick, Deactivation of alumina supported and unsupported PdO methane oxidation catalyst: the effect of water on sulfate poisoning, Appl. Catal. B Environ. 34 (2001) 287–297, https://doi.org/10.1016/S0926-3373(01)00222-3.
[64] P. Auvinen, J.T. Hirvi, N.M. Kinnunen, M. Suvanto, PdSO4 surfaces in methane oxidation catalysts: DFT studies on stability, reactivity, and water inhibition, ACS Catal. 10 (2020) 12943–12953, https://doi.org/10.1021/ACSCATAL.0C03686.
[65] R.J. Gorte, T. Luo, J.M. Vohs, An examination of sulfur poisoning on Pd/Ceria catalysts, J. Catal. 210 (2002) 397–404, https://doi.org/10.1006/jcat.2002.3689.
[66] S. Tan, D. Li, Enhancing catalytic activity of lanthanide oxysulfate ($La_2O_2O_4$/$Pr_2O_2SO_4$) via facile manipulation of nanoscale catalyst synthesis process and reactor configuration, Appl. Catal. A Gen. 544 (2017) 55–65, https://doi.org/10.1016/J.APCATA.2017.07.015.
[67] Y.G. Denisenko, V.V. Atuchin, M.S. Molokeev, A.E. Sedykh, N.A. Khritokhin, A. S. Aleksandrovsky, A.S. Oreshonkov, N.P. Shestakov, S.V. Adichtchev, A. M. Pugachev, E.I. Sal'nikova, O.V. Andreev, I.A. Razumkova, K. Müller-Buschbaum, Exploration of the crystal structure and thermal and spectroscopic properties of monoclinic praseodymium sulfate $Pr_2(SO_4)_3$, Molecules 27 (2022) 3966, https://doi.org/10.3390/molecules27133966.
[68] E. Sartoretti, C. Novara, A. Chiodoni, F. Giorgis, M. Piumetti, S. Bensaid, N. Russo, D. Fino, Nanostructured ceria-based catalysts doped with La and Nd: How acid-base sites and redox properties determine the oxidation mechanisms, Catal. Today 390–391 (2022) 117–134, https://doi.org/10.1016/J.CATTOD.2021.11.040.
[69] M. Waqif, P. Bazin, O. Saur, J.C. Lavalley, G. Blanchard, O. Touret, Study of ceria sulfation, Appl. Catal. B Environ. 11 (1997) 193–205, https://doi.org/10.1016/S0926-3373(96)00040-9.
[70] X. Zhang, Y. Liu, J. Deng, L. Jing, L. Wu, H. Dai, Catalytic performance and SO_2 resistance of zirconia-supported platinum-palladium bimetallic nanoparticles for methane combustion, Catal. Today 402 (2022) 138–148, https://doi.org/10.1016/j.cattod.2022.03.027.
[71] N.M. Kinnunen, J.T. Hirvi, K. Kallinen, T. Maunula, M. Keenan, M. Suvanto, Case study of a modern lean-burn methane combustion catalyst for automotive applications: what are the deactivation and regeneration mechanisms? Appl. Catal. B Environ. 207 (2017) 114–119, https://doi.org/10.1016/J.APCATB.2017.02.018.